Imprinted SARS-CoV-2 humoral immunity induces convergent Omicron RBD evolution

Yunlong Cao[1,2,#,*], Fanchong Jian[1,3,#], Jing Wang[1,4,#], Yuanling Yu[2,#], Weiliang Song[1,4,#], Ayijiang Yisimayi[1,4], Jing Wang[2], Ran An[2], Na Zhang[2], Yao Wang[2], Peng Wang[2], Lijuan Zhao[2], Haiyan Sun[2], Lingling Yu[2], Sijie Yang[1,5], Xiao Niu[1,3], Tianhe Xiao[1,6], Qingqing Gu[2], Fei Shao[2], Xiaohua Hao[7], Yanli Xu[7], Ronghua Jin[7], Youchun Wang[2,8,*], Xiaoliang Sunney Xie[1,2,*]

[1]Biomedical Pioneering Innovation Center (BIOPIC), Peking University, Beijing, P.R. China.

[2]Changping Laboratory, Beijing, P.R. China.

[3]College of Chemistry and Molecular Engineering, Peking University, Beijing, P.R. China.

[4]School of Life Sciences, Peking University, Beijing, P.R. China.

[5]Peking-Tsinghua Center for Life Sciences, Peking University, Beijing, P.R. China.

[6]Joint Graduate Program of Peking-Tsinghua-NIBS, Academy for Advanced Interdisciplinary Studies, Peking University, Beijing, China.

[7]Beijing Ditan Hospital, Capital Medical University, Beijing, P.R. China.

[8]Division of HIV/AIDS and Sex-transmitted Virus Vaccines, Institute for Biological Product Control, National Institutes for Food and Drug Control (NIFDC), Beijing, P.R. China.

[*]Correspondence: Youchun Wang (wangyc@nifdc.org.cn); Xiaoliang Sunney Xie (sunneyxie@biopic.pku.edu.cn); Yunlong Cao (yunlongcao@pku.edu.cn).

[#]These authors contributed equally.

Abstract

Continuous evolution of Omicron has led to numerous subvariants that exhibit growth advantage over BA.5. Such rapid and simultaneous emergence of variants with enormous advantages is unprecedented. Despite their rapidly divergent evolutionary courses, mutations on their receptor-binding domain (RBD) converge on several hotspots, including R346, K356, K444, L452, N460K and F486. The driving force and destination of such convergent evolution and its impact on humoral immunity established by vaccination and infection remain unclear. Here, we demonstrate that these convergent mutations can cause striking evasion of convalescent plasma, including those from BA.5 breakthrough infection, and existing antibody drugs, including Evusheld and Bebtelovimab. BR.2, CA.1, BQ.1.1, BM.1.1.1, and especially XBB, are the most antibody-evasive strain tested, far exceeding BA.5 and approaching SARS-CoV-1 level. To delineate the origin of the convergent evolution, we determined the escape mutation profiles and neutralization activity of monoclonal antibodies (mAbs) isolated from BA.2 and BA.5 breakthrough-infection convalescents. Importantly, due to humoral immune imprinting, BA.2 and especially BA.5 breakthrough infection caused significant reductions in the epitope diversity of neutralizing antibodies and increased proportion of non-neutralizing mAbs, which in turn concentrated humoral immune pressure and promoted the convergent RBD evolution. Additionally, the precise convergent RBD mutations and evolution trends of BA.2.75/BA.5 subvariants could be inferred by integrating the neutralization-weighted DMS profiles of mAbs from various immune histories (3051 mAbs in total). Moreover, we demonstrated that as few as five additional convergent mutations based on BA.5 or BA.2.75 could completely evade most plasma samples, including those from BA.5 breakthrough infection, while retaining sufficient hACE2-binding affinity. These results suggest that current herd immunity and BA.5 vaccine boosters may not provide sufficiently broad protection against infection. Broad-spectrum SARS-CoV-2 vaccines and NAb drugs development should be of high priority, and the constructed convergent mutants could serve to examine their effectiveness in advance.

Main

50 SARS-CoV-2 Omicron BA.1, BA.2, and BA.5 have demonstrated strong neutralization evasion capability, posing severe challenges to the efficacy of existing humoral immunity established through vaccination and infection [1-15]. Nevertheless, Omicron is continuously evolving, leading to various new subvariants, including BA.2.75 and BA.4.6 [16-22]. Importantly, a high proportion of these emerging variants display significant growth advantages over BA.5, such as BA.2.3.20,
55 BA.2.75.2, CA.1, BR.2, BN.1, BM.1.1.1, BU.1, BQ.1.1, and XBB (Fig. 1a) [23]. Such rapid and simultaneous emergence of multiple variants with enormous growth advantages is unprecedented. Notably, although these derivative subvariants appear to diverge along the evolutionary course, the mutations they carry on the receptor-binding domain (RBD) converge on the same sites, including R346, K444, V445, G446, N450, L452, N460, F486, F490, and
60 R493 (Fig. 1b, Extended Data Fig. 1). Most mutations on these residues are known to be antibody-evasive, as revealed by deep mutational scanning (DMS) [1,2,24-26]. It's crucial to examine the impact of these convergent mutations on antibody-escaping capability, receptor binding affinity, and the efficacy of vaccines and antibody therapeutics. It's also important to investigate the driving force behind this accelerated emergence of RBD mutations, what such
65 mutational convergence would lead to, and how we can prepare for such convergent RBD evolution.

Convergent RBD evolution causes extensive immune evasion

First, we tested the antibody evasion capability of these convergent variants. We constructed the VSV-based spike-pseudotyped virus of Omicron BA.2, BA.2.75, and BA.4/5 sublineages
70 carrying those convergent mutations and examined the neutralizing activities of therapeutic neutralizing antibodies (NAbs) against them (Fig. 2a and Extended Data Fig. 2a) [13,27-32]. The COV2-2196+COV2-2130 (Evusheld) [28,33] is vulnerable to F486, R346, and K444-G446 mutations, evaded or highly impaired by BJ.1 (R346T), XBB (R346T+V445P+F486S), BA.2.75.2/CA.1/BM.1.1/BM.1.1.1 (R346T+F486S), BR.2 (R346T+F486I), BA.4.6.1
75 (R346T+F486V), BA.5.6.2/BQ.1 (K444T+F486V), BU.1 (K444M+F486V), and BQ.1.1 (R346T+K444T+F486V). LY-CoV1404 (Bebtelovimab) remains potent against BF.16 (K444R) and BA.5.1.12 (V445A) but shows reduced potency against BA.5.5.1 (N450D) [31] (Extended

Data Fig. 2a). Importantly, LY-CoV1404 was escaped by BJ.1, XBB, BR.1, and BQ.1.1 while exhibiting strongly reduced activity against BA.2.38.1, BA.5.6.2, and BQ.1 due to K444N/T mutations and the combination of K444M/G446S or V445P/G446S [31]. SA55+SA58 is a pair of broad NAbs isolated from vaccinated SARS convalescents that target non-competing conserved epitopes [2,32]. SA58 is weak to G339H and R346T mutations and showed reduced neutralization efficacy against BJ.1/XBB and BA.2.75 sublineages. SA55 is the only NAb demonstrating high potency against all tested Omicron subvariants. Among the tested variants, XBB and BQ.1.1 exhibited the strongest resistance to therapeutic mAbs and cocktails (Fig. 2a). Since the SA55+SA58 cocktail is still in preclinical development, the efficacy of available antibody drugs, including the BA.2.75/BA.5-effective Evusheld and Bebtelovimab, are extensively affected by the emerging subvariants with convergent mutations.

Sufficient ACE2-binding affinity is essential for SARS-CoV-2 variants to gain advantages in transmission. Thus, we examined the relative hACE2 binding affinity of these variants by evaluating hACE2 neutralizing potency against the pseudoviruses. The higher neutralizing efficacy of soluble hACE2 indicates a higher ACE2-binding affinity [18]. Overall, these convergent variants all demonstrate sufficient ACE2-binding affinity, at least higher than D614G, allowing their prevalence, including the most evasive XBB, BM.1.1.1, BR.2, CA.1, and BQ.1.1 (Fig. 2b and Extended Data Fig. 2b). Specifically, R493Q reversion increases the binding affinity to hACE2, which is consistent with previous reports [4,18,20]. K417T shows a moderate increase in binding affinity to hACE2. In contrast, F486S, K444M, and K444N have a clear negative impact on binding affinity, while K444T does not cause significant impairment of ACE2 binding. These observations are also in line with previous DMS results [34].

Most importantly, we investigated how these variants escape the neutralization of plasma samples from individuals with various immune histories. We recruited cohorts of individuals who received 3 doses of CoronaVac [35] with or without breakthrough infection by BA.1, BA.2, or BA.5. Convalescent plasma samples were collected around 4 weeks after hospital discharge (Supplementary Table 1). Plasma from CoronaVac vaccinees was obtained two weeks after the third dose. There was a significant reduction in the NT50 against most tested BA.2, BA.2.75, or BA.5 subvariants, compared to that against corresponding ancestral BA.2, BA.2.75, or BA.5,

respectively (Fig. 2c-f and Extended Data Fig. 2c-f). BJ.1, BA.2.10.4, and BA.2.3.20 are highly immune evasive. Plasma of vaccinees and BA.1/BA.2/BA.5 convalescents neutralize these three subvariants with similar NT50 (Fig. 2c-e). Newly emerging BA.2.75 and BA.5 subvariants also demonstrated strong antibody-evading capability. BA.5 subvariants with R346T, K444T/R, and V445A exhibit a similar reduction in NT50, while N450D is slightly less evasive than others (Extended Data Fig. 2c-f). BA.2.75 subvariants with L452R, R346T, K356T, K444M, and F490S exhibit further immune evasion as well. Importantly, BA.2.75.2 (BA.2.75+R346T+F486S), BM.1.1 (BA.2.75+R346T+F486S), BM.1.1.1 (BM.1.1+F490S), CA.1 (BA.2.75.2+L452R+T604I) in BA.2.75 sublineages, and BU.1 (BA.5+Y144del+K444M+N460K), BQ.1.1 (BA.5+R346T+K444T+N460K) in BA.5 sublineages, are among the most humoral immune evasive strain tested. CA.1 causes a reduction in NT50 of plasma from 3-dose vaccinees, BA.1 breakthrough infection, BA.2 breakthrough infection, and BA.5 breakthrough infection by 4.3, 7.6, 8.8, and 3.4 folds compared to BA.2.75, respectively. BQ.1.1 reduces the NT50 of the plasma from the four cohorts by 3.0, 3.9, 4.4 and 6.4 folds compared to BA.5, respectively. NT50 of BA.5 convalescents against BQ.1.1 is higher than that against CA.1, which is probably contributed by the strong capability of BA.2.75 subvariants to evade NTD-targeting antibodies (Fig. 2f). Strikingly, the BJ.1/BM.1.1.1 recombinant strain XBB showed the most extreme immune evasion ability, displaying comparable NT50 to SARS-CoV-1. These observations demonstrate that convergent RBD evolution could cause significant immune escape at a scale never seen before. Such rapid and convergent emergence of antibody-escaping variants, especially when they can evade convalescent plasma from BA.5 breakthrough infection, suggests that vaccine boosters designed based on BA.5 may not achieve broad-spectrum protection against infection.

Immune imprinting induces convergent RBD evolution

It is crucial to investigate the origin of such accelerated RBD convergent evolution. Therefore, we characterized the antibody repertoires induced by Omicron BA.2 and BA.5 breakthrough infection, which is the dominant immune background of current global herd immunity. Following the strategy described in our previous report using PBMC from BA.1 breakthrough infection [2], we enriched antigen-specific memory B cells by fluorescence-activated cell sorting

(FACS) for individuals who had recovered from BA.2 and BA.5 breakthrough infection (Supplementary Table 1). RBD-binding $CD27^{+}/IgM^{-}/IgD^{-}$ cells were subjected to single-cell V(D)J sequencing (scVDJ-seq) to determine the BCR sequences (Extended Data Figure 3a-c).

Similar to that reported in BA.1 breakthrough infection, immune imprinting, or so-called "original antigenic sin", is also observed in BA.2 and BA.5 breakthrough infection [2,36-39]. Post-vaccination infection with BA.2 and BA.5 mainly recalls cross-reactive memory B cells elicited by wildtype-based vaccine, but rarely produces BA.2/BA.5 specific B cells, similar to BA.1 breakthrough infection (Fig. 3a-b). This is in marked contrast to Omicron infection without previous vaccination (Fig. 3c). The RBD-targeting antibody sequences determined by scVDJ-seq are then expressed *in vitro* as human IgG1 monoclonal antibodies (mAbs). As expected, only a small proportion of the expressed mAbs specifically bind to BA.2/BA.5 RBD and are not cross-reactive to WT RBD, determined by enzyme-linked immunosorbent assay (ELISA), concordant with the FACS results (Fig. 3d). Importantly, cross-reactive mAbs exhibit significantly higher somatic hypermutation (SHM), indicating that these antibodies are more affinity-matured and are most likely recalled from previously vaccination-induced memory (Fig. 3d).

Next, we determined the escape mutation profiles of these antibodies by high-throughput DMS and measured their neutralizing activities against SARS-CoV-2 D614G, BA.2, BA.5, and BA.2.75 (Fig. 3e, Extended Data Fig. 4a-b). Previously, we reported the DMS profiles and the epitope distribution of antibodies isolated from WT vaccinated/infected individuals, SARS-CoV-2 vaccinated SARS convalescents, and BA.1 convalescents, which could be classified into 12 epitope groups [2]. Among them, mAbs in groups A, B, C, D1, D2, F2, and F3 compete with ACE2 and exhibit neutralizing activity (Extended Data Fig. 5a-d, 6a-d); while mAbs in groups E1, E2.1, E2.2, E3, and F1 do not compete with ACE2 (Extended Data Fig. 7a-c). Antibodies in groups E2.2, E3, and F1 exhibit low or no neutralizing capability (Extended Data Fig. 4b, 7d). To integrate the previous dataset with DMS profiles of the new mAbs isolated from BA.2 and BA.5 convalescents, we co-embedded all antibodies using multidimensional scaling (MDS) based on their DMS profiles, followed by *t*-distributed stochastic neighbor embedding (*t*-SNE) for visualization, and used KNN-based classification to determine the

epitope groups of new mAbs (Fig. 3e). This results in a dataset containing the DMS profiles of 3051 SARS-CoV-2 WT RBD-targeting mAbs in total (Supplementary Table 2). The epitope distribution of mAbs from BA.2 breakthrough infection is generally similar to those elicited by BA.1, except for the increased proportion of mAbs in group C (Fig. 3f). However, BA.5-elicited mAbs showed a more distinct distribution compared to BA.1, with a significantly increased proportion of mAbs in group D2 and E2.2, and decreased ratio of antibodies in groups B and E2.1. The main reason is that the F486 and L452 mutations carried by BA.5 make these cross-reactive memory B cells unable to be activated and recalled (Fig. 3f, Extended Data Fig. 5b, 6a and 7a). Remarkably, antibody repertoires induced by all Omicron breakthrough infections are distinct from those stimulated by WT. Compared to WT infection or vaccination, BA.1, BA.2, and BA.5 breakthrough infection mainly elicit mAbs of group E2.2, E3, and F1, which do not compete with ACE2 and demonstrate weak neutralizing activity, while WT-elicited antibodies enrich mAbs of groups A, B, and C which compete with ACE2 and exhibit strong neutralization potency (Fig. 3g-h). Strikingly, the combined proportion of E2.2, E3, and F1 antibodies rose from 29% in WT convalescents/vaccinees, 53% in BA.1 convalescents, 51% in BA.2 convalescents, to 63% in BA.5 convalescents (Fig. 3f). Overall, the proportion and diversity of neutralizing antibody epitopes are reduced in Omicron breakthrough infection, especially in BA.5 breakthrough infection.

To better delineate the impact of immune imprinting and consequent reduction of NAb epitope diversity on the RBD evolutionary pressure, we aggregated the DMS profiles of large collections of mAbs to estimate the impact of mutations on the efficacy of humoral immunity, as inspired by previous works (Supplementary Table 2) [40]. It is essential to incorporate the effects of ACE2 binding, RBD expression, neutralizing activity of mAbs, and codon usage constraint to estimate the SARS-CoV-2 evolution trend on the RBD. In brief, each mutation on the RBD would have an impact on each mAb in the set, which is quantified by the escape scores determined by DMS and weighted by its IC50 against the evolving strain. For each residue, only those amino acids that are accessible by one nucleotide mutation are included. Impacts on ACE2-binding affinity and RBD expression of each mutation are also considered in the analyses, using data determined by DMS in previous reports [34,41,42]. Finally, the estimated

relative preference of each mutation is calculated using the sum of weighted escape scores of all mAbs in the specific set.

The reduced NAb epitope diversity caused by imprinted humoral response could be strikingly shown by the estimated mutation preference spectrum (Fig. 4a). Diversified escaping-score peaks, which also represent immune pressure, could be observed when using BA.2-elicited antibodies, while only two major peaks could be identified, R346T/S and K444E/Q/N/T/M, when using BA.5-elicited antibodies (Fig. 4a). Interestingly, these two hotspots are the most frequently mutated sites in continuously evolving BA.4/5 subvariants, and convergently occurred in multiple lineages (Fig. 1a-b and Extended Data Fig. 1). Similar analysis for WT and BA.1 also demonstrated diversified peaks; thus, the concentrated immune pressure strikingly reflects the reduced diversity of NAbs elicited by BA.5 breakthrough infection due to immune imprinting, and these concentrated preferred mutations highly overlapped with convergent hotspots observed in the real world (Extended Data Fig. 8a-b). Together, our results indicate that due to immune imprinting, BA.5 breakthrough infection caused significant reductions of NAb epitope diversity and increased proportion of non-neutralizing mAbs, which in turn concentrated immune pressure and promoted the convergent RBD evolution.

Accurate inference of RBD evolution hotspots

Moreover, we wonder if the real-world evolutionary trends of SARS-CoV-2 RBD could be rationalized and even predicted by aggregating this large DMS dataset containing mAbs from various immune histories. Using the mAbs elicited from WT vaccinees or convalescents weighted by IC50 against the D614G strain, we identified mutation hotspots including K417N/T, K444-G446, N450, L452R, and especially E484K (Extended Data Fig. 8a). Most of these residues were mutated in previous VOCs, such as K417N/E484K in Beta, K417T/E484K in Gamma, L452R in Delta, and G446S/E484A in Omicron BA.1, confirming our estimation and inference. Evidence of the emergence of BA.2.75 and BA.5 could also be found using WT, BA.1, and BA.2-elicited mAbs with IC50 against BA.2, where peaks on 444-446, 452, 460, and 486 could be identified (Extended Data Fig. 8c). To better investigate the evolution trends of BA.2.75 and BA.5, the two major lineages circulating currently, we then included antibodies

elicited by various immune background, including WT/BA.1/BA.2/BA.5 convalescents, which we believe is the best way to represent the current heterogeneous global humoral immunity (Fig. 4b and Extended Data Fig. 8d). For BA.2.75, the most significant sites are R346T/S, K356T, N417Y/H/I/T, K444E/Q/N/T/M, V445D/G/A, N450T/D/K/S, L452R, I468N, A484P, F486S/V, and F490S/Y. We noticed that these identified residues, even most specific mutations, highly overlapped with recent mutation hotspots of BA.2.75 (Fig. 1b). Two exceptions are A484 and F490, which are feature residues of Group C and could be replaced by L452R and F486S/V (Extended Data Fig. 5c). I468N mutation is also highly associated with K356 mutations, and its function could be covered by K356T (Extended Data Fig. 7a-b). Due to stronger antibody evasion, the preference spectrum of BA.5 is much more concentrated compared to BA.2.75, but the remaining sites are highly overlapped and complementary with BA.2.75. The most striking residues are R346, K444-G446, and N450, followed by K356, N417, L455, N460, and A484. As expected, L452R/F486V does not stand out in BA.5 preference spectrum, while N460K harbored by BA.2.75 appears. These sites and mutations are also popular in emerging BA.4/5 subvariants, proving that our RBD evolution inference system works accurately.

Convergent evolution could eventually nullify plasma neutralization

It is important to examine where this convergence evolution would lead to. Based on the observed and predicted convergent hotpots on RBD of BA.2.75 and BA.5, we wonder if we could construct the convergent variants in advance and investigate to what extent they will evade the humoral immune response. To do this, we must first evaluate the antibody evasion capability of the convergent mutations and their combinations. Thus, we selected a panel of 178 NAbs from 8 epitope groups that could potently neutralize BA.2 and determined their neutralizing activity against constructed mutants carrying single or multiple convergent mutations (Fig. 4c and Extended Data Fig. 9a). NAbs from F1-F3 epitope groups were not included since they are either completely escaped by BA.2 or too rare in Omicron infected convalescents (Fig. 3f). As expected, R493Q and N417T are not major contributors to antibody evasion, but R493Q significantly benefits ACE2 binding. Most group A NAbs are sensitive to N460K, and BA.5+N460K escapes the majority of NAbs in group A due to the combination of

F486V and N460K. All NAbs in group B are escaped by F486S/V. Group C NAbs are heavily escaped by F490S and are strongly affected by L452R and F486S/V. A part of group C NAbs is also slightly affected by K444N/T and N450D. G446S affects a part of the D1/D2 NAbs, as previously reported (Extended Data Fig. 6a-b) [20]. D1/D2 NAbs are more susceptible to K444N/T, V445A and N450D, and some D1 NAbs could also be escaped by L452R (Extended Data Fig. 6a-b). E1 is mainly affected by R346T, D339H and K356T (Extended Data Fig. 6c). E2.1 and E2.2 exhibit similar properties, evaded by K356T, R346T and L452R (Extended Data Fig. 7a-b). E3 antibodies seem not significantly affected by any of the constructed mutants, as expected (Extended Data Fig. 7c), but they generally exhibit very low neutralization (Extended Data Fig. 7d). BA.5+R346T escapes most antibodies in D1, E1, and E2.1/E2.2, and an additional K444N further escapes most mAbs in D2, demonstrating the feasibility and effectiveness of combining convergent mutations to achieve further evasion. Importantly, adding six mutations to BA.5 could achieve the evasion of the vast majority of RBD NAbs, while maintaining high hACE2-binding affinity, despite the reduction caused by K444N/T and F486V. Together, these findings indicate the feasibility of generating a heavy-antibody-escaping mutant harboring accumulated convergent escape mutations while maintaining sufficient hACE2-binding affinity (Fig. 4c and Extended Data Fig. 9a).

Although the proportion of Omicron-specific mAbs is low due to immune imprinting, it is still necessary to evaluate their neutralization potency and breadth, especially against the convergent mutants. We tested the neutralizing activity of a panel of Omicron-specific RBD-targeting mAbs against D614G, BA.1, BA.2, BA.5, BA.2.75, BA.2.75.2, BR.1, BR.2, CA.1, BQ.1.1 and XBB. These mAbs were isolated from convalescent plasma with Omicron breakthrough infection (Fig. 4d). They could bind RBD of the corresponding exposed Omicron variant but do not cross-bind WT RBD, as confirmed by ELISA. We found these mAbs could effectively neutralize against the exposed strain, as expected, but exhibited poor neutralizing breadth, which means their potency would be largely impaired by other Omicron subvariants, consistent with our previous discovery [2]. Notably, BQ.1.1 and XBB could escape most of these Omicron-specific NAbs. Thus, these Omicron-specific antibodies would not effectively expand the breadth of the antibody repertoire of Omicron breakthrough infection when facing

280 convergent variants.

We then evaluated the potency of NTD-targeting NAbs against BA.2, BA.4/5, BA.2.75 and their sublineages and constructed mutants with selected NTD mutations using a panel of 14 NTD-targeting NAbs, as it is reported that NTD-targeting antibodies are abundant in plasma from BA.2 breakthrough infection and contribute to cross-reactivity [43]. Most selected
285 mutations are from recently designated Omicron subvariants, except for R237T, which was near V83A, designed to escape mAbs targeting an epitope reported recently [20]. None of the NTD-targeting NAbs exhibit strong neutralizing potency, and the IC50 values are all over 0.2 μg/mL [44,45] (Fig. 4e and Extended Data Fig. 9b). We found the tested BA.2-effective NTD-targeting NAbs could be separated into two clusters, named group α and δ in our previous
290 report, respectively [20] (Extended Data Fig. 9c). NAbs in group α target the well-known antigenic supersite on NTD [46], which is sensitive to K147E and W152R harbored by BA.2.75*, and Y144del harbored by BJ.1/XBB; while the other group δ is affected by V83A (XBB) and R237T. The other three NTD mutations harbored by BA.2.75, F157L, I210V and G257S did not significantly affect the tested mAbs, consistent with previous sera neutralization data [18].
295 Two of the NTD mutations harbored by BJ.1 or XBB, Y144del and V83A, each escapes a cluster of them and together would enable XBB to exhibit extremely strong capability of escaping NTD-targeting NAbs.

Based on the above results, we designed multiple VSV-based pseudoviruses that gradually gain convergent mutations that could induce RBD/NTD-targeting NAb resistance (Fig. 5a). The
300 constructed final mutant contains 11 additional mutations on the NTD and RBD compared to BA.5, or 9 mutations compared to BA.2.75. The neutralizing activities of Omicron-effective NAb drugs were first evaluated. As expected, the majority of existing effective NAb drugs, except SA55, are escaped by these mutants (Fig. 5b). Similarly, we also determined the ACE2-binding capability of these mutants by neutralization assays using hACE2 (Fig. 5c). Although
305 some of the designed pseudoviruses, especially those with K444N and F486V, exhibit reduced activity to hACE2 compared to original BA.2.75 or BA.5 variants, their binding affinities are still higher than that of D614G (Fig. 2b). Importantly, our designed pseudoviruses could largely

evade the plasma of vaccinees and convalescents after BA.1 breakthrough infection, BA.2 breakthrough infection, and even BA.5 breakthrough infection (Fig. 5d-g). Among the
310 derivative mutants of BA.2.75, L452R, K444M, R346T, and F486V contribute mainly to the significant reduction in neutralization (Fig. 5d-g). Adding more NTD mutations does not contribute to stronger evasion in BA.2.75-based mutants, but we observed a significant reduction in NT50 of BA.2/BA.5 convalescents against BA.5-based mutants with K147E+W152R, suggesting BA.2/BA.5 convalescent plasma contains a large proportion of
315 NTD-targeting antibodies [43]. As the NTD of BA.1 differs from that of BA.2 and BA.5, we did not observe significant effects of NTD mutations on the efficacy of BA.1 convalescent plasma. Plasma neutralization titers of most vaccinees and convalescents decreased to the lower detection limit against BA.2.75 with 5 extra RBD mutations L452R, K444M, R346T, F486V, and K356T. The same applies to vaccinees or BA.1 convalescents against BA.5 with 4 extra
320 RBD mutations K444N, R346T, N460K, and K356T. The plasma from BA.2/BA.5 convalescents can tolerate more mutations based on BA.5, and extra NTD mutations such as K147E and W152R are needed to completely eliminate their neutralization. Together, we demonstrate that as few as five additional mutations on BA.5 or BA.2.75 could completely evade most plasma samples, including those from BA.5 breakthrough infection, while
325 maintaining high hACE2-binding affinity. Similar efforts have been made in a recent report despite different construction strategies [47]. The constructed evasive mutants, such as BA.2.75-S5/6/7/8 and BA.5-S7/8, could serve to examine the effectiveness of broad-spectrum vaccines and NAbs in advance.

Discussion

330 In this work, we showed that convergent RBD evolution can cause severe immune evasion and could be rationalized by integrating DMS profiles. Given the existence of immune imprinting, the humoral immune repertoire is not effectively diversified by infection with new Omicron variants, while the immune pressure on the RBD becomes increasingly concentrated and promotes convergent evolution. The interaction between convergent evolution of escaping
335 variants and less diversified antibody repertoire would ultimately lead to a highly evasive variant, posing a great challenge to current vaccines and antibody drugs.

Notably, the antibody evasion capability of CA.1, BQ.1.1, XBB, and the constructed convergent mutants have already reached or even exceeded SARS-CoV-1, indicating extensive antigenicity drift (Fig. 5d-g). Indeed, by constructing an antigenic map of the tested SARS-CoV-2/SARS-CoV-1 variants using the plasma NT50 data, we found that the antigenicity distances of SARS-CoV-2 ancestral strain to CA.1, XBB and BQ.1.1 are already comparable to that of SARS-CoV-1 (Extended Data Fig. 10a). Given that there are ~50 different amino acids between SARS-CoV-1 and SARS-CoV-2 RBD, but only 21 mutations on BQ.1.1 RBD compared to the ancestral strain, these results indicate that the global pandemic indeed has greatly promoted the efficiency of the virus to evolve immune escape mutations.

Additionally, since these convergent variants could escape the binding of the majority of NAbs, it is possible that infections by those mutants may hardly revoke pre-existing memory B cells that encode NAbs, but only recall those memory B cells that encode non-neutralizing antibodies. This may cause inabilities to induce rapid increase of plasma neutralization after infection and may correlate with escalated percentages of severe symptoms. Therefore, the disease severity caused by new convergent variants needs to be closely monitored.

Finally, our prediction demonstrated a remarkable consistency with real-world observations. Some variants close to the predicted and constructed variants have already emerged while we performed the experiments, validating our prediction model. For example, BQ.1.1, BA.5+R346T+K444T+N460K, is highly similar to BA.5-S3, BA.5+R346T+N417T+K444N+N460K, given that K444N/T and K417N/T exhibit similar evasion capabilities (Fig. 4c). If we have this prediction model at the beginning of the pandemic, the development of NAb drugs and vaccines may not be so frustrated against the continuously emerging SARS-CoV-2 variants. Broad-spectrum SARS-CoV-2 vaccines and NAb drugs development should be of high priority, and the constructed convergent mutants could serve to examine their effectiveness in advance.

Data and Code Availability

Processed mutation escape scores and custom scripts to analyze the data can be downloaded at https://github.com/jianfcpku/convergent_RBD_evolution. Sequences and neutralization of the antibodies are included in Supplementary Table 2. Any other raw data of specific antibodies are available from the corresponding authors upon request. We used vdj_GRCh38_alts_ensembl-5.0.0 as the reference of V(D)J alignment, which can be obtained from https://support.10xgenomics.com/single-cell-vdj/software/downloads/latest. IMGT/DomainGapAlign is based on the built-in lastest IMGT antibody database, and we let the "Species" parameter as "Homo sapiens" while keeping the others as default.

Acknowledgments

We thank J. Bloom for his gift of the yeast SARS-CoV-2 RBD libraries. We thank all volunteers for providing the blood samples. This project is financially supported by the Ministry of Science and Technology of China and Changping laboratory under the project number (CPL-1233).

Author contributions

Y.C. designed the study. X.S.X supervised the study. Y.C, F.J., A.Y, Q.G. and X.S.X. wrote the manuscript with inputs from all authors. A.Y., W.S., R.A., Yao.W., and X.N. performed B cell sorting, single-cell VDJ sequencing, and antibody sequence analyses. J.W. (BIOPIC), H.S. and F.J. performed and analyzed the DMS data. Y.Y. and Youchun.W. constructed the pseudotyped virus. N.Z., P.W., L.Y., T.X. and F.S. performed the pseudotyped virus neutralization assays. W.S. and Y.C. analyzed the neutralization data. X.H., Y.X., and R.J. recruited the SARS-CoV-2 vaccinees and convalescents. J.W. (Changping Laboratory), L.Y. and F.S. performed the antibody expression.

Conflicts of interest

X.S.X and Y.C. are co-founders of Singlomics Biopharmaceuticals and listed as inventors on patents related to DXP-604, SA55, and SA58. The remaining authors declare no competing interests.

Main Figures

Fig. 1 | Convergent evolution of Omicron RBD with growth advantage over BA.5.

a, Whole-genome maximum likelihood phylogenetic analysis of Omicron subvariants. Variants with a growth advantage over the original BA.5 are colored. Relative growth advantage values are calculated using the CoV-Spectrum website. **b**, Key RBD mutations in emerging SARS-CoV-2 BA.5 and BA.2.75 subvariants exhibit convergent patterns.

Fig. 2 | Emerging Omicron subvariants further evade neutralizing antibodies.

a, IC50 of therapeutic NAbs against VSV-based pseudoviruses with spike glycoproteins of emerging SARS-CoV-2 BA.2/BA.5/BA.2.75 subvariants. green, IC50 ⩽ 100ng/mL; white, 100ng/mL < IC50 < 1,000ng/mL; red, IC50 ⩾ 1,000ng/mL; *, IC50 ⩾ 10,000ng/mL. **b**, Relative hACE2-binding affinity measured by IC50 of hACE2 against pseudoviruses of variants. Error bars indicate mean±s.d. P-values were calculated using two-tailed Wilcoxon's rank-sum test. *, $p < 0.05$; **, $p < 0.01$; ***, $p < 0.001$. No label on variants with $p > 0.05$. Variants with significantly higher affinity are colored blue, while those with lower affinity are colored red. **c-f**, Pseudovirus-neutralizing titers against SARS-CoV-2 D614G and Omicron subvariants of plasma from vaccinated individuals or convalescents of breakthrough infection. **c**, Individuals who had received 3 doses of CoronaVac (n = 40). **d**, Convalescents who had been infected with BA.1 after receiving 3 doses of CoronaVac (n = 50). **e**, Convalescents who had been infected with BA.2 after receiving 3 doses of CoronaVac (n = 39). **f**, Convalescents who had been infected with BA.5 after receiving 3 doses of CoronaVac (n = 21). The geometric mean titers are labeled. Statistical tests are performed using two-tailed Wilcoxon signed-rank tests of paired samples. *, $p < 0.05$; **, $p < 0.01$; ***, $p < 0.001$; NS, not significant, $p > 0.05$.

Fig. 3 | Epitope characterization of mAbs from Omicron breakthrough convalescents.

a-c, FACS analysis of pooled memory B cells (IgM^-, $IgD^-/CD27^+$) from Omicron convalescents. **a**, BA.5 breakthrough infection; **b**, BA.2 breakthrough infection; **c**, BA.2 convalescents without vaccination. **d**, The heavy chain variable domain SHM rate of BCRs from BA.2 breakthrough infection convalescents that bind BA.2 RBD but not WT RBD, and that are cross-reactive to WT/BA.2-RBD, and BCRs from BA.5 breakthrough infection convalescents that

bind BA.5 RBD but not WT RBD, and that are cross-reactive to WT/BA.5 RBD. Binding specificity is determined by ELISA. Statistical tests are determined using two-tailed Wilcoxon signed-rank tests. Boxes display the 25th percentile, median and 75th percentile, and violin plots show kernel density estimation curves of the distribution. **e**, t-SNE and clustering of SARS-CoV-2 wildtype RBD-binding antibodies based on DMS profiles of 3051 antibodies. **f**, Epitope distribution of 680 antibodies from wildtype convalescents, 652 antibodies from post-vaccination BA.1 infection convalescents, 600 from BA.2 breakthrough infection convalescents, and 238 from BA.5 breakthrough infection convalescents. **g**, Neutralizing activity against SARS-CoV-2 D614G (n=3046), BA.2.75 (n=3045), and BA.4/5 (n=3044), respectively; and **h**, ACE2 competition level determined by competition ELISA (n=1316), were projected onto the t-SNE.

Fig. 4 | Immune imprinting promotes convergent evolution of escape mutations.

a-b, Normalized average escape scores weighted by IC50 against **a**, BA.2/BA.5 pseudovirus using DMS profiles of mAbs from corresponding convalescents. **b**, BA.2.75/BA.5 pseudovirus using DMS profiles of all mAbs except those from SARS convalescents. **c**, IC50 of representative potent BA.2-neutralizing antibodies in epitope group A, B, C, D1, D2, E1, E2.1, E2.2, and E3, against multiple emerging and constructed Omicron subvariants with escape mutations, in addition to IC50 of hACE2 against these variants. Error bars indicate mean±s.d. P-values were calculated using two-tailed Wilcoxon's rank-sum test. *, $p < 0.05$; **, $p < 0.01$; ***, $p < 0.001$. No label on variants with $p > 0.05$. Variants with significantly higher affinity are colored blue, while those with lower affinity are colored red. **d**, IC50 against featured Omicron subvariants of RBD-targeting mAbs from BA.1 (N=108), BA.2 (N=92), and BA.5 (N=17) breakthrough convalescents, which bind the RBD of the elicited strain but not WT. Binding specificity is determined by ELISA. The geometric mean IC50s are labeled, and error bars indicate the geometric standard deviation. P-values are calculated using two-tailed Wilcoxon signed-rank tests compared to the corresponding strain. *, $p < 0.05$; **, $p < 0.01$; ***, $p < 0.001$; NS, not significant, $p > 0.05$. **e**, IC50 of NTD-targeting mAbs against emerging Omicron subvariants and BA.2 mutants with single NTD substitution.

Fig. 5 | Accumulation of convergent escape mutations leads to complete loss of neutralization.

a, Mutations of multiple designed mutants that harbor key convergent escape mutations based on BA.2.75 and BA.5. **b**, IC50 of therapeutic mAbs and cocktails against pseudoviruses of designed mutants. green, IC50 ≤ 100ng/mL; white, 100ng/mL < IC50 < 1,000ng/mL; red, IC50 ≥ 1,000ng/mL; *, IC50 ≥ 10,000ng/mL. **c**, IC50 of hACE2 against the designed mutants. Error bars indicate mean±s.d. P-values were calculated using two-tailed Wilcoxon's rank-sum test. *, $p < 0.05$; **, $p < 0.01$; ***, $p < 0.001$. No label on variants with $p > 0.05$. **d-g**, Pseudovirus neutralizing titers against SARS-CoV-2 D614G, Omicron subvariants and designed mutants of plasma from vaccinated or convalescent individuals from breakthrough infection. **d**, Individuals who received 3 doses of CoronaVac (n = 40). **e**, Convalescents infected with BA.1 after receiving 3 doses of CoronaVac (n = 50). **f**, Convalescents infected with BA.2 after receiving 3 doses of CoronaVac (n = 39). **g**, Convalescents infected with BA.5 after receiving 3 doses of CoronaVac (n = 21). Key additional mutations harbored by each designed mutant are annotated above the points. The geometric mean titers are labeled. P-values are determined using two-tailed Wilcoxon signed-rank tests of paired samples. *, $p < 0.05$; **, $p < 0.01$; ***, $p < 0.001$; NS, not significant, $p > 0.05$. Statistical tests are determined using two-tailed Wilcoxon signed-rank tests.

Extended Data Figures

Extended Data Fig. 1 | Mutations on the spike glycoprotein of recently emerging Omicron subvariants.

Red grids indicate the corresponding PANGO lineage carries the corresponding mutation.

Extended Data Fig. 2 | Antibody evasion of previous VOCs and other emerging Omicron variants.

a, IC50 of therapeutic NAbs against pseudoviruses of additional emerging SARS-CoV-2 Omicron subvariants. **b**, Relative hACE2-binding affinity measured by IC50 of hACE2 against

pseudoviruses. **c-f**, NT50 against SARS-CoV-2 previous variants of concern and additional Omicron subvariants of plasma from vaccinated individuals or convalescents of breakthrough infection. Data of variants shown in Fig. 2c-f are shown here again for comparison. All antibody or plasma samples, statistical methods and meaning of labels are the same as that in Fig. 2.

Extended Data Fig. 3 | FACS gating strategy for isolating antibodies from BA.2 and BA.5 convalescents.

a, FACS gating strategy of antigen-specific B cells from individuals who recovered form BA.5 breakthrough infection. **b**, FACS gating strategy of antigen-specific B cells from individuals who recovered from BA.2 breakthrough infection. **c**, FACS gating strategy of antigen-specific B cells from individuals who recovered from BA.2 infection (no SARS-CoV-2 vaccination history). Gating region of WT RBD^+ in BA.2 or BA.5 RBD^+ is consistent with that of WT RBD^+ in $CD27^+$, IgM^-, IgD^- population, as shown in the second line of each figure. For convenience, Fig. 2a-c are also included here.

Extended Data Fig. 4 | Distribution of antibody sources and neutralizing activities on the DMS landscape.

a, Sources of the 3051 mAbs involved in this study projected on the t-SNE of DMS profiles. **b**, IC50 against SARS-CoV-1 (N=1870 determined), Omicron BA.1 (N=2933), and BA.2 (N=3044) of these mAbs projected on the embedding.

Extended Data Fig. 5 | Escape hotspots and neutralization of mAbs in epitope groups A, B and C

a-c, Average escape scores of epitope group A (**a**), B (**b**), C (**c**) and on each RBD residue are projected onto the structure of SARS-CoV-2 RBD (PDB: 6M0J). And average escape maps at escape hotspots of antibodies, grouped by their sources, in epitope groups A (**a**), B (**b**) and C (**c**), and corresponding sequence alignment of SARS-CoV-2 WT and Omicron RBDs. The height of each amino acid in the escape maps represents its mutation escape score. Mutated sites in Omicron variants are marked in bold. **d**, Pseudovirus-neutralizing IC50 of antibodies

in group A, B, and C, from wildtype convalescents or vaccinees (WT-elicited, n=133, 50, 106 for A-C, respectively), BA.1 convalescents (BA.1-elicited, n=51, 49, 24), BA.2 convalescents (BA.2-elicited, n=34, 36, 56) and BA.5 convalescents (BA.5-elicited, n=16, 6, 14). The geometric mean IC50 are labeled, and error bars indicate the geometric standard deviation. P-values are calculated using two-tailed Wilcoxon signed-rank tests. *, $p < 0.05$; **, $p < 0.01$; ***, $p < 0.001$; NS, not significant, $p > 0.05$.

Extended Data Fig. 6 | Escape hotspots and neutralization of mAbs in epitope group D and E1

a-d, Similar to Extended Data Fig. 3, but for epitope groups D1, D2, and E1. **d**, For WT-elicited mAbs, n=49, 37, 19 for D1, D2 and E1, respectively; For BA.1-elicited, n=59, 21, 14; For BA.2-elicited, n=56, 15, 9; For BA.5-elicited, n=14, 17, 9.

Extended Data Fig. 7 | Escape hotspots and neutralization of mAbs in epitope group E2 and E3

a-d, Similar to Extended Data Fig. 3 and 4, but for epitope groups E2.1, E2.2, and E3. **d**, For WT-elicited mAbs, n=35, 69, 63 for E2.1, E2.2 and E3, respectively; For BA.1-elicited, n=81, 159, 89; For BA.2-elicited, n=53, 132, 106; For BA.5-elicited, n=11, 85, 36.

Extended Data Fig. 8 | Predicted escape hotspots of SARS-CoV-2 variants

a, Normalized average escape scores weighted by IC50 against D614G using DMS profiles of mAbs from ancestral strain infection or vaccination with a logo plot showing specific mutations on important residues. **b**, Normalized average escape scores of mAbs from BA.1 breakthrough infection, weighted by IC50 against BA.1. **c**, Normalized average escape scores of mAbs from ancestral strain infection or vaccination and BA.1 breakthrough infection, weighted by IC50 against BA.2. Including BA.2-elicited mAbs does not cause substantial change. **d**, WT/BA.1/BA.2-elicited mAbs with IC50 against BA.2.75 and BA.5, similar to Fig. 4b.

Extended Data Fig. 9 | IC50 heatmaps of representative mAbs against constructed Omicron variants.

525 **a**, Color shades indicate IC50 of antibodies (columns) against constructed Omicron BA.2 or BA.5 subvariants (rows) carrying mutations on the epitope of each group. The order of mAbs is the same as in Figure 4c. **b**, IC50 of NTD-targeting antibodies against SARS-CoV-2 variants, which is related to Fig. 4e.

Extended Data Fig. 10 | Antigenic map shows the convergent evolution from BA.2.75 and
530 **BA.5**

a, Antigenic map of SARS-CoV-2 variants constructed using plasma neutralization data by principal component analysis (PCA). **b**, Antigenic map of SARS-CoV-2 variants with constructed Omicron subvariants added

535 **Methods**

Isolation of peripheral blood mononuclear cells and plasma

Samples from vaccinees and individuals who had recovered from BA.1, BA.2, or BA.5 infection were obtained under study protocols approved by Beijing Ditan Hospital, Capital Medical University (Ethics committee archiving No. LL-2021-024-02) and the Tianjin
540 Municipal Health Commission, and the Ethics Committee of Tianjin First Central Hospital (Ethics committee archiving No. 2022N045KY). All donors provided written informed consent for the collection of information, the use of blood and blood components, and the publication of data generated from this study. Whole blood samples were diluted 1:1 with PBS+2% FBS (Gibco) and subjected to Ficoll (Cytiva) gradient centrifugation. Plasma was collected from the
545 upper layer. Cells were collected at the interface and further prepared by centrifugation, red blood cell lysis (Invitrogen eBioscience) and washing steps. The date of vaccination, hospitalization and sampling can be found in Supplementary Table 1.

BCR sequencing, analysis, and antibody production.

CD19+ B cells were isolated from PBMCs with EasySep Human CD19 Positive Selection Kit
550 II (STEMCELL, 17854). Every 10^6 B cells in 100 μl solution were stained with 3 μl FITC anti-

human CD20 antibody (BioLegend, 302304, clone: 2H7), 3.5 µl Brilliant Violet 421 anti-human CD27 antibody (BioLegend, 302824, clone: O323), 2 µl PE/Cyanine7 anti-human IgM antibody (BioLegend, 314532, clone: MHM-88), 2 µl PE/Cyanine7 anti-human IgD antibody (BioLegend, 348210, clone: IA6-2), 0.13 µg biotinylated SARS-CoV-2 BA.2 RBD protein (customized from Sino Biological) or 0.13 µg biotinylated SARS-CoV-2 BA.5 RBD protein (customized from Sino Biological) conjugated with PE-streptavidin (BioLegend, 405204) or APC-streptavidin (BioLegend, 405207), 0.13 µg SARS-CoV-2 WT biotinylated RBD protein (Sino Biological, 40592-V27H-B) conjugated with Brilliant Violet 605 Streptavidin (BioLegend, 405229). Cells are also labeled with biotinylated RBD conjugated to DNA-oligo-streptavidin. Cells were washed twice after 30 minutes of incubation on ice. 7-AAD (Invitrogen, 00-6993-50) was used to label dead cells. 7-AAD−CD20+CD27+IgM−IgD− SARS-CoV-2 BA.2 RBD+ or BA.5+ cells were sorted with a MoFlo Astrios EQ Cell Sorter. FACS data were analyzed using FlowJo v10.8 (BD Biosciences).

Sorted B cells were resuspended in appropriate volume and then processed with Chromium Next GEM Single Cell V(D)J Reagent Kits v1.1 following the manufacturer's user guide (10x Genomics, CG000208). Gel beads-in-emulsion (GEMs) were obtained with a 10X Chromium controller. GEMs were subjected to reverse transcription and purification. Reverse transcription products were subject to preamplification and purification with SPRIselect Reagent Kit (Beckman Coulter, B23318). BCR sequences (paired V(D)J) were enriched with 10X BCR primers. After library preparation, libraries were sequenced with Illumina sequencing platform.

10X Genomics V(D)J sequencing data were assembled as BCR contigs and aligned using Cell Ranger (v6.1.1) pipeline according to the GRCh38 BCR reference. Only the productive contigs and the B cells with one heavy chain and one light chain were kept for quality control. The germline V(D)J gene identification and annotation were performed by IgBlast (v1.17.1)[48]. Somatic hypermutation sites in the antibody variable domain were detected using Change-O toolkit (v1.2.0)[49].

Antibody heavy and light chain genes were optimized for human cell expression and

synthesized by GenScript. VH and VL were inserted separately into plasmids (pCMV3-CH, pCMV3-CL or pCMV3-CK) through infusion (Vazyme, C112). Plasmids encoding the heavy chain and light chain of antibodies were co-transfected by polyethylenimine-transfection to Expi293F™ cell (ThermoFisher, A14527). Cells were cultured at 36.5℃, 5% CO2, 175 rpm for 6-10 days. Supernatants containing mAbs were collected, and the supernatants were further purified with protein A magnetic beads (Genscript, L00695).

High-throughput mutation escape profiling

High-throughput mutation escape profiling platform has been described previously[1,2]. Briefly, deep mutation scanning libraries were constructed by mutagenesis PCR based on the Wuhan-Hu-1 RBD sequence (GenBank: MN908947, residues N331-T531). A unique 26-nucleotide (N26) barcode was appended to each RBD variant in mutant libraries by PCR, and the correspondence between the N26 barcode and mutations in RBD variants was acquired by PacBio sequencing. RBD mutant libraries were first transformed in the EBY100 strain of *Saccharomyces cerevisiae* and then enriched for properly folded ACE2 binders, which were used for subsequent mutation escape profiling. The above ACE2 binders were grown in SG-CAA media (2% w/v d-galactose, 0.1% w/v dextrose (d-glucose), 0.67% w/v yeast nitrogen base, 0.5% w/v casamino acids (−ade, −ura, −trp), 100 mM phosphate buffer, pH 6.0) at room temperature for 16-18h with agitation. Then these yeast cells were washed twice and proceeded to three rounds of magnetic beads-based selection. Obtained yeast cells after sequential sorting were recovered overnight in SD-CAA media (2% w/v dextrose (d-glucose), 0.67% w/v yeast nitrogen base, 0.5% w/v casamino acids (−ade, −ura, −trp), 70 mM citrate buffer, pH 4.5). Pre- and post-sort yeast populations were submitted to plasmid extraction by 96 Well Plate Yeast Plasmid Preps Kit (Coolaber, PE053). N26 barcode sequences were amplified with the extracted plasmid templates, and PCR products were purified and submitted to Illumina Nextseq 550 sequencing.

Antibody clustering and embedding based on DMS profiles

Data analysis of DMS was performed as described in previous reports [1,2]. In brief, the detected

barcode sequences of both the antibody-screened and reference library were aligned to the barcode-variant lookup table generated using dms_variants (v0.8.9). The escape scores of each variant X in the library were defined as $F\times(n_{X,ab} / N_{ab}) / (n_{X,ref} / N_{ref})$, where F is a scale factor to normalize the scores to the 0-1 range, while n and N are the number of detected barcodes for variant X and total barcodes in post-selected (ab) or reference (ref) samples, respectively. The escape scores of each mutation were calculated by fitting an epistasis model as described previously [41,50].

Epitope groups of new antibodies not included in our previous report are determined by k-nearest neighbors (KNN)-based classification. In brief, site escape scores of each antibody are first normalized and considered as a distribution across RBD residues, and only residues whose standard derivation is among the highest 50% of all residues are retained for further analysis. Then the dissimilarity or distance of two antibodies is defined by the Jessen-Shannon divergence of the normalized escape scores. Pair-wise dissimilarities of all antibodies in the dataset are calculated using the scipy package (scipy.spatial.distance.jensenshannon, v1.7.0). For each antibody, 15 nearest neighbors whose epitope groups have been determined by unsupervised clustering in our previous paper are identified and simply voted to determine the group of the selected antibody. To project the dataset onto a 2D space for visualization, we performed MDS to represent each antibody in a 32-dimensional space, and then t-SNE to get the 2D representation, using sklearn.manifold.MDS and sklearn.manifold.TSNE (v0.24.2).

Calculation of the estimated preference of RBD mutations

Four different weights are included in the calculation, including the weight for ACE2-binding affinity, RBD expression, codon constraint, and neutralizing activity. Impact on ACE2-binding affinity and RBD expression of each mutation based on WT, BA.1 and BA.2 are obtained from public DMS results. And for BA.5 (BA.2+L452R+F486V+R493Q) and BA.2.75 (BA.2+D339H+G446S+N460K+R493Q), BA.2 results are used except for these mutated residues, whose scores for each mutant are subtracted by the score for the mutation in BA.5 or BA.2.75. As the reported values are log fold changes, the weight is simply defined by the exponential of reported values, i.e., $\exp[S_{\mathrm{bind}}]$ or $\exp[S_{\mathrm{expr}}]$, respectively. For codon

constraint, the weight is 1.0 for mutants that could be accessed by one nucleotide mutation, and 0.0 for others. We used the following RBD nucleotide sequences for determination of accessible mutants, WT/D614G (Wuhan-Hu-1 reference genome), BA.1 (EPI_ISL_10000028), BA.2 (EPI_ISL_10000005), BA.4/5 (EPI_ISL_11207535), BA.2.75 (EPI_ISL_13302209). For neutralizing activity, the weight is -$\log_{10}$(IC50). The IC50 values (μg/mL), which are smaller than 0.0005 or larger than 1.0 are considered as 0.0005 or 1.0, respectively. The raw escape scores for each antibody are first normalized by the max score among all mutants, and the final weighted score for each antibody and each mutation is the production of the normalized scores and four corresponding weights. The final mutation-specific weighted score is the summation of scores of all antibodies in the designated antibody set, and then normalized again to make it a value between 0 and 1. Logo plots for visualization of escape maps were generated by the Python package logomaker (v0.8).

Pseudotyped-virus assay

The Spike gene (GenBank: MN908947) was mammalian condon-optimized and inserted into the pcDNA3.1 vector. Site-directed mutagenesis PCR was performed as described previously[51]. The sequence of mutants is shown in Fig. S1. Pseudotyped viruses were generated by transfection 293T cells (ATCC, CRL-3216) with pcDNA3.1-Spike with Lipofectamine 3000 (Invitrogen). The cells were subsequently infected with G*ΔG-VSV (Kerafast) that packages expression cassettes for firefly luciferase instead of VSV-G in the VSV genome. The cell supernatants were discarded after 6-8h harvest and replaced with complete culture media. The cell was cultured one day and then the cell supernatant containing pseudotyped virus was harvested, filtered (0.45-μm pore size, Millipore), aliquoted, and stored at -80 °C. Viruses of multiple variants were diluted to the same number of copies before use.

mAbs or plasma was serially diluted and incubated with the pseudotyped virus in 96-well plates for 1 h at 37°C. Trypsin-treated Huh-7 cells (Japanese Collection of Research Bioresources, Cat0403) were added to the plate. The cells were cultured for 20-28 h in 5% CO_2, 37°C incubators. The supernatants were removed and left 100 μL in each well, and 100 μL luciferase substrate (Perkinelmer, 6066769) was added and incubated in the dark for 2 min. The cell lysate

was removed, and the chemiluminescence signals were collected by PerkinElmer Ensight. Each experiment was repeated at least twice.

Dulbecco's modified Eagle medium (DMEM, high glucose; HyClone) with 100 U/mL of penicillin-streptomycin solution (Gibco), 20 mM N-2-hydroxyethylpiperazine-N-2-ethane sulfonic acid (HEPES, Gibco) and 10% fetal bovine serum (FBS, Gibco) were used in cell culture. Trypsin-EDTA (0.25%, Gibco) was used to detach cells before seeding to the plate.

References

1 Cao, Y. *et al.* Omicron escapes the majority of existing SARS-CoV-2 neutralizing antibodies. *Nature* **602**, 657-663, doi:10.1038/s41586-021-04385-3 (2022).

2 Cao, Y. *et al.* BA.2.12.1, BA.4 and BA.5 escape antibodies elicited by Omicron infection. *Nature* **608**, 593-602, doi:10.1038/s41586-022-04980-y (2022).

3 Iketani, S. *et al.* Antibody evasion properties of SARS-CoV-2 Omicron sublineages. *Nature* **604**, 553-556, doi:10.1038/s41586-022-04594-4 (2022).

4 Wang, Q. *et al.* Antibody evasion by SARS-CoV-2 Omicron subvariants BA.2.12.1, BA.4 and BA.5. *Nature* **608**, 603-608, doi:10.1038/s41586-022-05053-w (2022).

5 Tuekprakhon, A. *et al.* Antibody escape of SARS-CoV-2 Omicron BA.4 and BA.5 from vaccine and BA.1 serum. *Cell* **185**, 2422-2433 e2413, doi:10.1016/j.cell.2022.06.005 (2022).

6 Uraki, R. *et al.* Characterization and antiviral susceptibility of SARS-CoV-2 Omicron/BA.2. *Nature*, doi:10.1038/s41586-022-04856-1 (2022).

7 Liu, L. *et al.* Striking antibody evasion manifested by the Omicron variant of SARS-CoV-2. *Nature* **602**, 676-681, doi:10.1038/s41586-021-04388-0 (2022).

8 Cele, S. *et al.* Omicron extensively but incompletely escapes Pfizer BNT162b2 neutralization. *Nature* **602**, 654-656, doi:10.1038/s41586-021-04387-1 (2022).

9 Cameroni, E. *et al.* Broadly neutralizing antibodies overcome SARS-CoV-2 Omicron antigenic shift. *Nature* **602**, 664-670, doi:10.1038/s41586-021-04386-2 (2022).

10 Yamasoba, D. *et al.* Virological characteristics of the SARS-CoV-2 Omicron BA.2 spike. *Cell* **185**, 2103-2115 e2119, doi:10.1016/j.cell.2022.04.035 (2022).

11 Nutalai, R. *et al.* Potent cross-reactive antibodies following Omicron breakthrough in vaccinees. *Cell* **185**, 2116-2131 e2118, doi:10.1016/j.cell.2022.05.014 (2022).

12 Dejnirattisai, W. *et al.* SARS-CoV-2 Omicron-B.1.1.529 leads to widespread escape from neutralizing antibody responses. *Cell* **185**, 467-484 e415, doi:10.1016/j.cell.2021.12.046 (2022).

13 Cui, Z. *et al.* Structural and functional characterizations of infectivity and immune evasion of SARS-CoV-2 Omicron. *Cell* **185**, 860-871 e813, doi:10.1016/j.cell.2022.01.019 (2022).

14 Wang, K. *et al.* Memory B cell repertoire from triple vaccinees against diverse SARS-CoV-2 variants. *Nature* **603**, 919-925, doi:10.1038/s41586-022-04466-x (2022).

15 Kimura, I. *et al.* Virological characteristics of the SARS-CoV-2 Omicron BA.2 subvariants including BA.4 and BA.5. *Cell*, doi:10.1016/j.cell.2022.09.018 (2022).

16 Shu, Y. & McCauley, J. GISAID: Global initiative on sharing all influenza data – from vision to reality. *Eurosurveillance* **22**, 30494, doi:doi:https://doi.org/10.2807/1560-7917.ES.2017.22.13.30494

(2017).
17 Rambaut, A. *et al.* A dynamic nomenclature proposal for SARS-CoV-2 lineages to assist genomic epidemiology. *Nature Microbiology* **5**, 1403-1407, doi:10.1038/s41564-020-0770-5 (2020).
18 Wang, Q. *et al.* Antigenic characterization of the SARS-CoV-2 Omicron subvariant BA.2.75. *Cell Host & Microbe*, doi:https://doi.org/10.1016/j.chom.2022.09.002 (2022).
19 Sheward, D. J. *et al.* Evasion of neutralising antibodies by omicron sublineage BA.2.75. *Lancet Infect Dis*, doi:10.1016/S1473-3099(22)00524-2 (2022).
20 Cao, Y. *et al.* Characterizations of enhanced infectivity and antibody evasion of Omicron BA.2.75. *bioRxiv*, 2022.2007.2018.500332, doi:10.1101/2022.07.18.500332 (2022).
21 Jian, F. *et al.* Further humoral immunity evasion of emerging SARS-CoV-2 BA.4 and BA.5 subvariants. *bioRxiv*, 2022.2008.2009.503384, doi:10.1101/2022.08.09.503384 (2022).
22 Saito, A. *et al.* Virological characteristics of the SARS-CoV-2 Omicron BA.2.75. *bioRxiv*, 2022.2008.2007.503115, doi:10.1101/2022.08.07.503115 (2022).
23 Chen, C. *et al.* CoV-Spectrum: Analysis of Globally Shared SARS-CoV-2 Data to Identify and Characterize New Variants. *Bioinformatics* **38**, 1735-1737, doi:10.1093/bioinformatics/btab856 (2021).
24 Greaney, A. J. *et al.* Comprehensive mapping of mutations in the SARS-CoV-2 receptor-binding domain that affect recognition by polyclonal human plasma antibodies. *Cell Host Microbe* **29**, 463-476 e466, doi:10.1016/j.chom.2021.02.003 (2021).
25 Greaney, A. J. *et al.* Complete Mapping of Mutations to the SARS-CoV-2 Spike Receptor-Binding Domain that Escape Antibody Recognition. *Cell Host Microbe* **29**, 44-57 e49, doi:10.1016/j.chom.2020.11.007 (2021).
26 Greaney, A. J. *et al.* Mapping mutations to the SARS-CoV-2 RBD that escape binding by different classes of antibodies. *Nature Communications* **12**, 4196, doi:10.1038/s41467-021-24435-8 (2021).
27 Copin, R. *et al.* The monoclonal antibody combination REGEN-COV protects against SARS-CoV-2 mutational escape in preclinical and human studies. *Cell* **184**, 3949-3961 e3911, doi:10.1016/j.cell.2021.06.002 (2021).
28 Zost, S. J. *et al.* Potently neutralizing and protective human antibodies against SARS-CoV-2. *Nature* **584**, 443-449, doi:10.1038/s41586-020-2548-6 (2020).
29 Self, W. H. *et al.* Efficacy and safety of two neutralising monoclonal antibody therapies, sotrovimab and BRII-196 plus BRII-198, for adults hospitalised with COVID-19 (TICO): a randomised controlled trial. *Lancet Infectious Diseases* **22**, 622-635, doi:10.1016/S1473-3099(21)00751-9 (2022).
30 Pinto, D. *et al.* Cross-neutralization of SARS-CoV-2 by a human monoclonal SARS-CoV antibody. *Nature* **583**, 290-295, doi:10.1038/s41586-020-2349-y (2020).
31 Westendorf, K. *et al.* LY-CoV1404 (bebtelovimab) potently neutralizes SARS-CoV-2 variants. *Cell Rep* **39**, 110812, doi:10.1016/j.celrep.2022.110812 (2022).
32 Cao, Y. *et al.* Rational identification of potent and broad sarbecovirus-neutralizing antibody cocktails from SARS convalescents. *bioRxiv*, 2022.2008.2003.499114, doi:10.1101/2022.08.03.499114 (2022).
33 Loo, Y. M. *et al.* The SARS-CoV-2 monoclonal antibody combination, AZD7442, is protective in nonhuman primates and has an extended half-life in humans. *Sci Transl Med* **14**, eabl8124, doi:10.1126/scitranslmed.abl8124 (2022).
34 Starr, T. N. *et al.* Deep mutational scans for ACE2 binding, RBD expression, and antibody escape in the SARS-CoV-2 Omicron BA.1 and BA.2 receptor-binding domains. *bioRxiv*, 2022.2009.2020.508745, doi:10.1101/2022.09.20.508745 (2022).

35 Gao, Q. *et al.* Development of an inactivated vaccine candidate for SARS-CoV-2. *Science* **369**, 77-81, doi:10.1126/science.abc1932 (2020).
36 Quandt, J. *et al.* Omicron BA.1 breakthrough infection drives cross-variant neutralization and memory B cell formation against conserved epitopes. *Sci Immunol* **7**, eabq2427, doi:10.1126/sciimmunol.abq2427 (2022).
37 Khan, K. *et al.* Omicron BA.4/BA.5 escape neutralizing immunity elicited by BA.1 infection. *Nature Communications* **13**, 4686, doi:10.1038/s41467-022-32396-9 (2022).
38 Park, Y. J. *et al.* Imprinted antibody responses against SARS-CoV-2 Omicron sublineages. *bioRxiv*, 2022.2005.2008.491108, doi:10.1101/2022.05.08.491108 (2022).
39 Reynolds, C. J. *et al.* Immune boosting by B.1.1.529 (Omicron) depends on previous SARS-CoV-2 exposure. *Science* **377**, eabq1841, doi:10.1126/science.abq1841 (2022).
40 Greaney, A. J., Starr, T. N. & Bloom, J. D. An antibody-escape estimator for mutations to the SARS-CoV-2 receptor-binding domain. *Virus Evol* **8**, veac021, doi:10.1093/ve/veac021 (2022).
41 Starr, T. N. *et al.* Deep Mutational Scanning of SARS-CoV-2 Receptor Binding Domain Reveals Constraints on Folding and ACE2 Binding. *Cell* **182**, 1295-1310 e1220, doi:10.1016/j.cell.2020.08.012 (2020).
42 Starr, T. N. *et al.* Shifting mutational constraints in the SARS-CoV-2 receptor-binding domain during viral evolution. *Science* **377**, 420-424, doi:10.1126/science.abo7896 (2022).
43 Muik, A. *et al.* Omicron BA.2 breakthrough infection enhances cross-neutralization of BA.2.12.1 and BA.4/BA.5. *Science Immunology* **0**, eade2283, doi:10.1126/sciimmunol.ade2283 (2022).
44 Wang, Z. *et al.* Analysis of memory B cells identifies conserved neutralizing epitopes on the N-terminal domain of variant SARS-Cov-2 spike proteins. *Immunity* **55**, 998-1012 e1018, doi:10.1016/j.immuni.2022.04.003 (2022).
45 Chi, X. *et al.* A neutralizing human antibody binds to the N-terminal domain of the Spike protein of SARS-CoV-2. *Science* **369**, 650-655, doi:doi:10.1126/science.abc6952 (2020).
46 McCallum, M. *et al.* N-terminal domain antigenic mapping reveals a site of vulnerability for SARS-CoV-2. *Cell* **184**, 2332-2347 e2316, doi:10.1016/j.cell.2021.03.028 (2021).
47 Witte, L. *et al.* Epistasis lowers the genetic barrier to SARS-CoV-2 neutralizing antibody escape. *bioRxiv*, 2022.2008.2017.504313, doi:10.1101/2022.08.17.504313 (2022).
48 Ye, J., Ma, N., Madden, T. L. & Ostell, J. M. IgBLAST: an immunoglobulin variable domain sequence analysis tool. *Nucleic Acids Res* **41**, W34-40, doi:10.1093/nar/gkt382 (2013).
49 Gupta, N. T. *et al.* Change-O: a toolkit for analyzing large-scale B cell immunoglobulin repertoire sequencing data. *Bioinformatics* **31**, 3356-3358, doi:10.1093/bioinformatics/btv359 (2015).
50 Otwinowski, J., McCandlish, D. M. & Plotkin, J. B. Inferring the shape of global epistasis. *Proc Natl Acad Sci U S A* **115**, E7550-E7558, doi:10.1073/pnas.1804015115 (2018).
51 Nie, J. *et al.* Quantification of SARS-CoV-2 neutralizing antibody by a pseudotyped virus-based assay. *Nat Protoc* **15**, 3699-3715, doi:10.1038/s41596-020-0394-5 (2020).

Figure 1

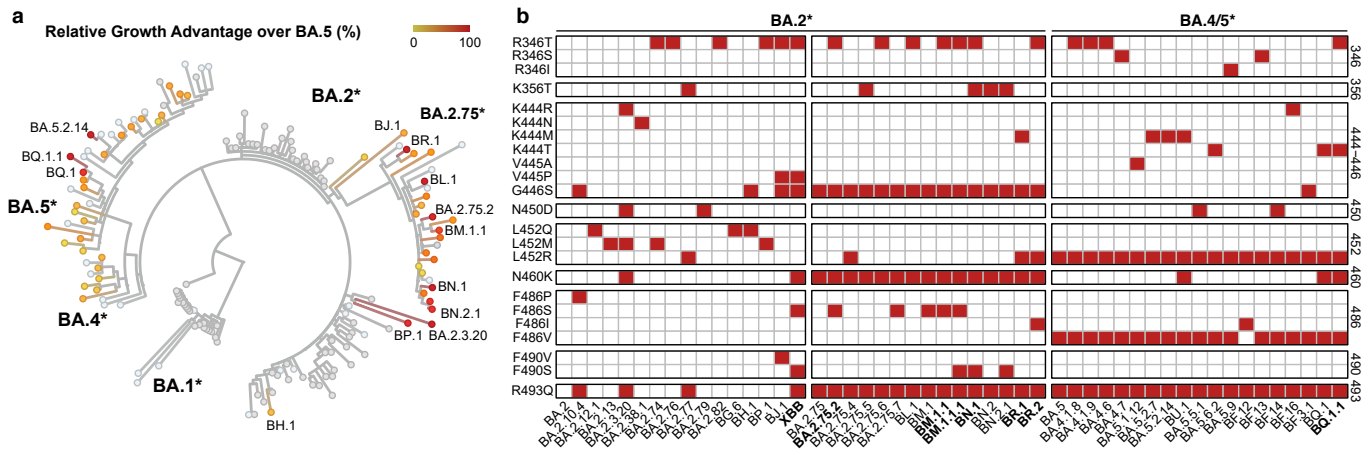

Fig. 1 | Convergent evolution of Omicron RBD with growth advantage over BA.5.
a, Whole-genome maximum likelihood phylogenetic analysis of Omicron subvariants. Variants with a growth advantage over the original BA.5 are colored. Relative growth advantage values are calculated using CoV-Spectrum website. b, Key RBD mutations in emerging SARS-CoV-2 BA.5 and BA.2.75 subvariants.

Figure 2

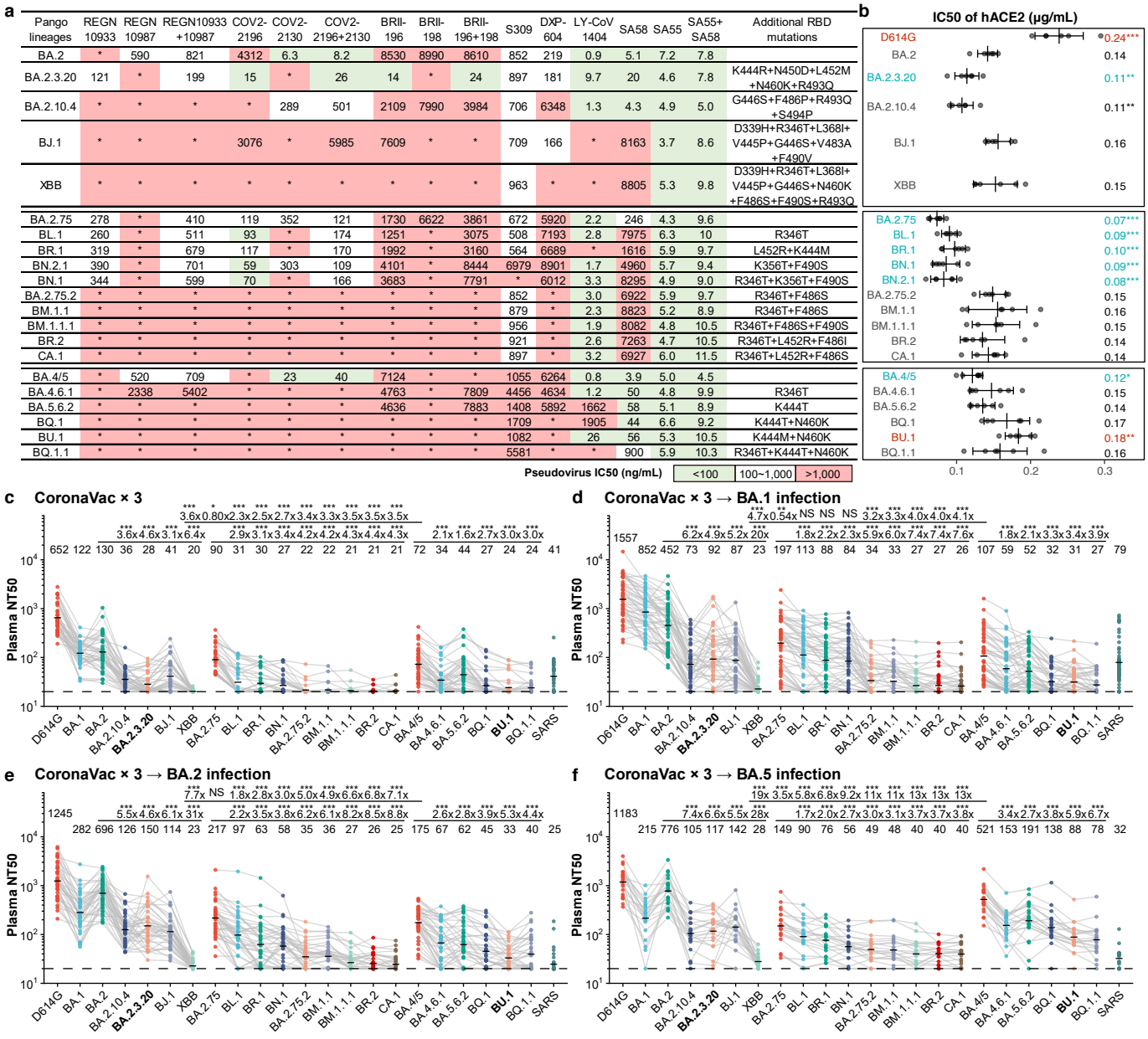

Pango lineages	REGN 10933	REGN 10987	REGN10933 +10987	COV2-2196	COV2-2130	COV2-2196+2130	BRII-196	BRII-198	BRII-196+198	S309	DXP-604	LY-CoV 1404	SA58	SA55	SA55+ SA58	Additional RBD mutations
BA.2	*	590	821	4312	6.3	8.2	8530	8990	8610	852	219	0.9	5.1	7.2	7.8	
BA.2.3.20	121	*	199	15	*	26	14	*	24	897	181	9.7	20	4.6	7.8	K444R+N450D+L452M +N460K+R493Q
BA.2.10.4	*	*	*	*	289	501	2109	7990	3984	706	6348	1.3	4.3	4.9	5.0	G446S+F486P+R493Q +S494P
BJ.1	*	*	*	3076	*	5985	7609	*	*	709	166	*	8163	3.7	8.6	D339H+R346T+L368I+ V445P+G446S+V483A +F490V
XBB	*	*	*	*	*	*	*	*	*	963	*	*	8805	5.3	9.8	D339H+R346T+L368I+ V445P+G446S+N460K +F486S+F490S+R493Q
BA.2.75	278	*	410	119	352	121	1730	6622	3861	672	5920	2.2	246	4.3	9.6	
BL.1	260	*	511	93	*	174	1251	*	3075	508	7193	2.8	7975	6.3	10	R346T
BR.1	319	*	679	117	*	170	1992	*	3160	564	6689	*	1616	5.9	9.7	L452R+K444M
BN.2.1	390	*	701	59	303	109	4101	*	8444	6979	8901	1.7	4960	5.7	9.4	K356T+F490S
BN.1	344	*	599	70	*	166	3683	*	7791	*	6012	3.3	8295	4.9	9.0	R346T+K356T+F490S
BA.2.75.2	*	*	*	*	*	*	*	*	*	852	*	3.0	6922	5.9	9.7	R346T+F486S
BM.1.1	*	*	*	*	*	*	*	*	*	879	*	2.3	8823	5.2	8.9	R346T+F486S
BM.1.1.1	*	*	*	*	*	*	*	*	*	956	*	1.9	8082	4.8	10.5	R346T+F486S+F490S
BR.2	*	*	*	*	*	*	*	*	*	921	*	2.6	7263	4.7	10.5	R346T+L452R+F486I
CA.1	*	*	*	*	*	*	*	*	*	897	*	3.2	6927	6.0	11.5	R346T+L452R+F486S
BA.4/5	*	520	709	*	23	40	7124	*	*	1055	6264	0.8	3.9	5.0	4.5	
BA.4.6.1	*	2338	5402	*	*	*	4763	*	7809	4456	4634	1.2	50	4.8	9.9	R346T
BA.5.6.2	*	*	*	*	*	*	4636	*	7883	1408	5892	1662	58	5.1	8.9	K444T
BQ.1	*	*	*	*	*	*	*	*	*	1709	*	1905	44	6.6	9.2	K444T+N460K
BU.1	*	*	*	*	*	*	*	*	*	1082	*	26	56	5.3	10.5	K444M+N460K
BQ.1.1	*	*	*	*	*	*	*	*	*	5581	*	*	900	5.9	10.3	R346T+K444T+N460K

Fig. 2 | Emerging Omicron subvariants further evade neutralizing antibodies.
a, IC50 of therapeutic NAbs against VSV-based pseudoviruses with spike glycoproteins of emerging SARS-CoV-2 BA.2/BA.5/BA.2.75 subvariants. green, IC50 ≤ 100ng/mL; white, 100ng/mL < IC50 < 1,000ng/mL; red, IC50 ≥ 1,000ng/mL; *, IC50 ≥ 10,000ng/mL. b, Relative hACE2-binding affinity measured by IC50 of hACE2 against pseudoviruses of variants. Error bars indicate mean±s.d. P-values were calculated using two-tailed Wilcoxon's rank-sum test. *, $p < 0.05$; **, $p < 0.01$; ***, $p < 0.001$. No label on variants with $p > 0.05$. Variants with significantly higher affinity are colored blue, while those with lower affinity are colored red. c-f, Pseudovirus-neutralizing titers against SARS-CoV-2 D614G and Omicron subvariants of plasma from vaccinated individuals or convalescents of breakthrough infection. c, Individuals who had received 3 doses of CoronaVac (n = 40). d, Convalescents who had been infected with BA.1 after receiving 3 doses of CoronaVac (n = 50). e, Convalescents who had been infected with BA.2 after receiving 3 doses of CoronaVac (n = 39). f, Convalescents who had been infected with BA.5 after receiving 3 doses of CoronaVac (n = 21). The geometric mean titers are labeled. Statistical tests are performed using two-tailed Wilcoxon signed-rank tests of paired samples. *, $p < 0.05$; **, $p < 0.01$; ***, $p < 0.001$; NS, not significant, $p > 0.05$.

Figure 3

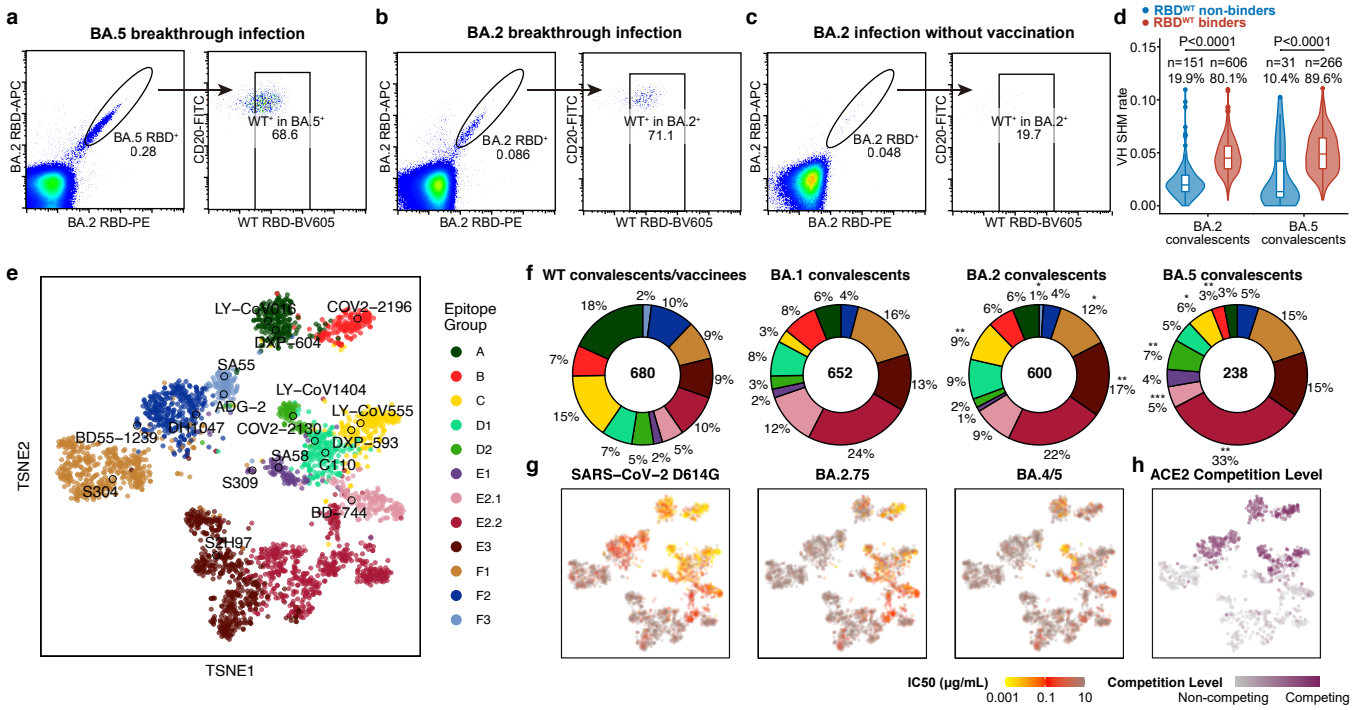

Fig. 3 | Epitope characterization of mAbs from Omicron breakthrough convalescents.
a-c, FACS analysis of pooled memory B cells (IgM-, IgD-/CD27+) from Omicron convalescents. a, BA.5 breakthrough infection; b, BA.2 breakthrough infection; c, BA.2 convalescents without vaccination. d, The heavy chain variable domain SHM rate of BCRs from BA.2 breakthrough infection convalescents that bind BA.2 RBD but not WT RBD, and that are cross-reactive to WT/BA.2-RBD, and BCRs from BA.5 breakthrough infection convalescents that bind BA.5 RBD but not WT RBD, and that are cross-reactive to WT/BA.5 RBD. Binding specificity is determined by ELISA. Statistical test are determined using two-tailed Wilcoxon signed-rank tests. Boxes show 25th percentile, median and 75th percentile, and violin plots show kernel density estimation curves of the distribution. e, t-SNE and clustering of SARS-CoV-2 wildtype RBD-binding antibodies based on DMS profiles of 3051 antibodies. f, Epitope distribution of 680 antibodies from wildtype convalescents, 652 antibodies from post-vaccination BA.1 infection convalescents, 600 from BA.2 breakthrough infection convalescents, and 238 from BA.5 breakthrough infection convalescents. g, Neutralizing activity against SARS-CoV-2 D614G (n=3046), BA.2.75 (n=3045), and BA.4/5 (n=3044), respectively; and h, ACE2 competition level determined by competition ELISA (n=1316), were projected onto the t-SNE.

Figure 4

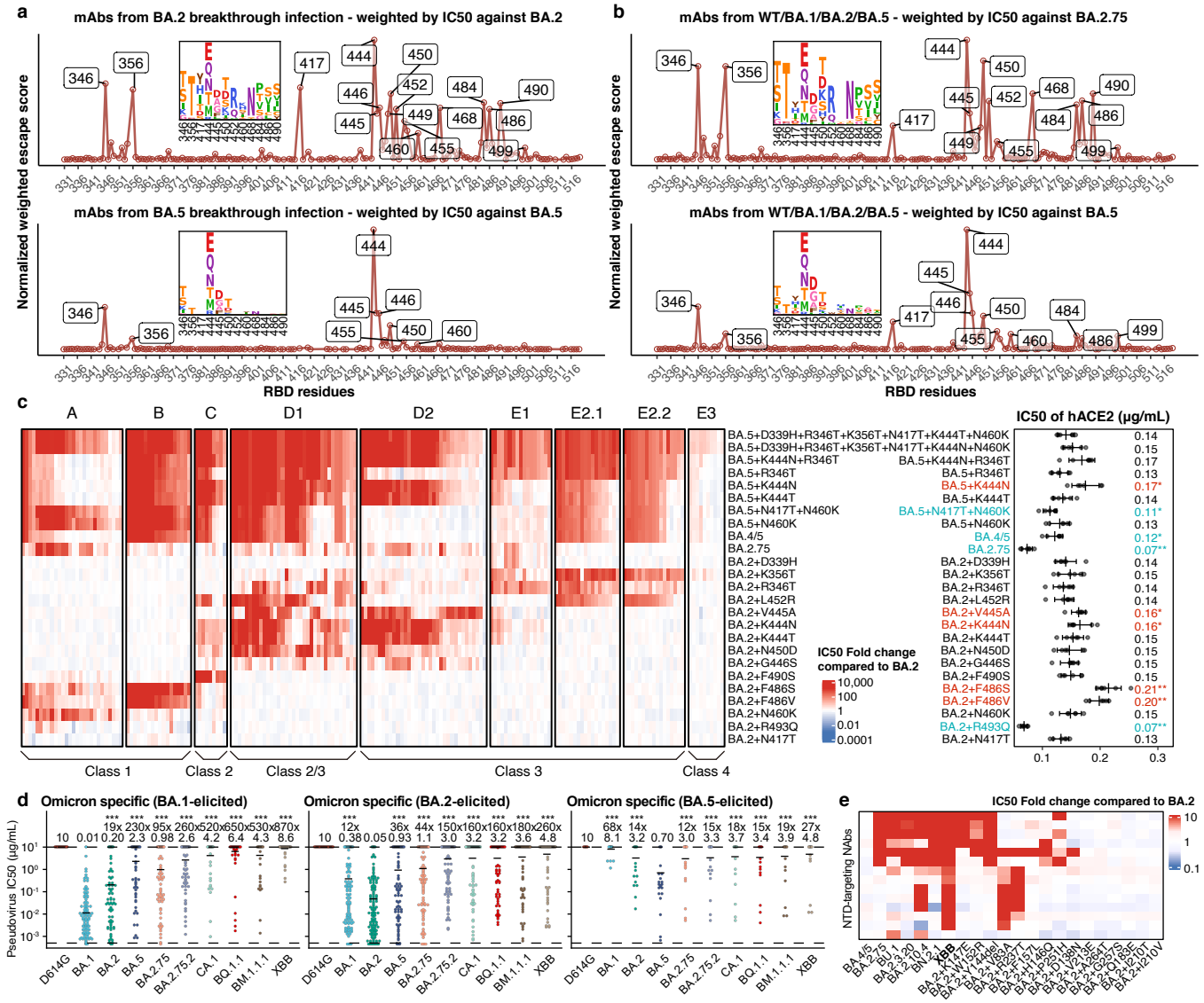

Fig. 4 | Immune imprinting promotes convergent evolution of escape mutations.
a-b, Normalized average escape scores weighted by IC50 against a, BA.2/BA.5 pseudovirus using DMS profiles of mAbs from corresponding convalescents. b, BA.2.75/BA.5 pseudovirus using DMS profiles of all mAbs except those from SARS convalescents. c, IC50 of representative potent BA.2-neutralizing antibodies in epitope group A, B, C, D1, D2, E1, E2.1, E2.2, and E3, against multiple emerging and constructed Omicron subvariants with escape mutations, in addition to IC50 of hACE2 against these variants. Error bars indicate mean±s.d. P-values were calculated using two-tailed Wilcoxon's rank-sum test. *, $p < 0.05$; **, $p < 0.01$; ***, $p < 0.001$. No label on variants with $p > 0.05$. Variants with significantly higher affinity are colored blue, while those with lower affinity are colored red. d, IC50 against featured Omicron subvariants of RBD-targeting mAbs from BA.1 (N=108), BA.2 (N=92), and BA.5 (N=17) breakthrough convalescents, which bind the RBD of the elicited strain but not WT. Binding specificity is determined by ELISA. The geometric mean IC50 are labeled, and error bars indicate geometric standard deviation. P-values are calculated using two-tailed Wilcoxon signed-rank tests compared to the corresponding strain. *, $p < 0.05$; **, $p < 0.01$; ***, $p < 0.001$; NS, not significant, $p > 0.05$. e, IC50 of NTD-targeting mAbs against emerging Omicron subvariants and BA.2 mutants with single NTD substitution.

Figure 5

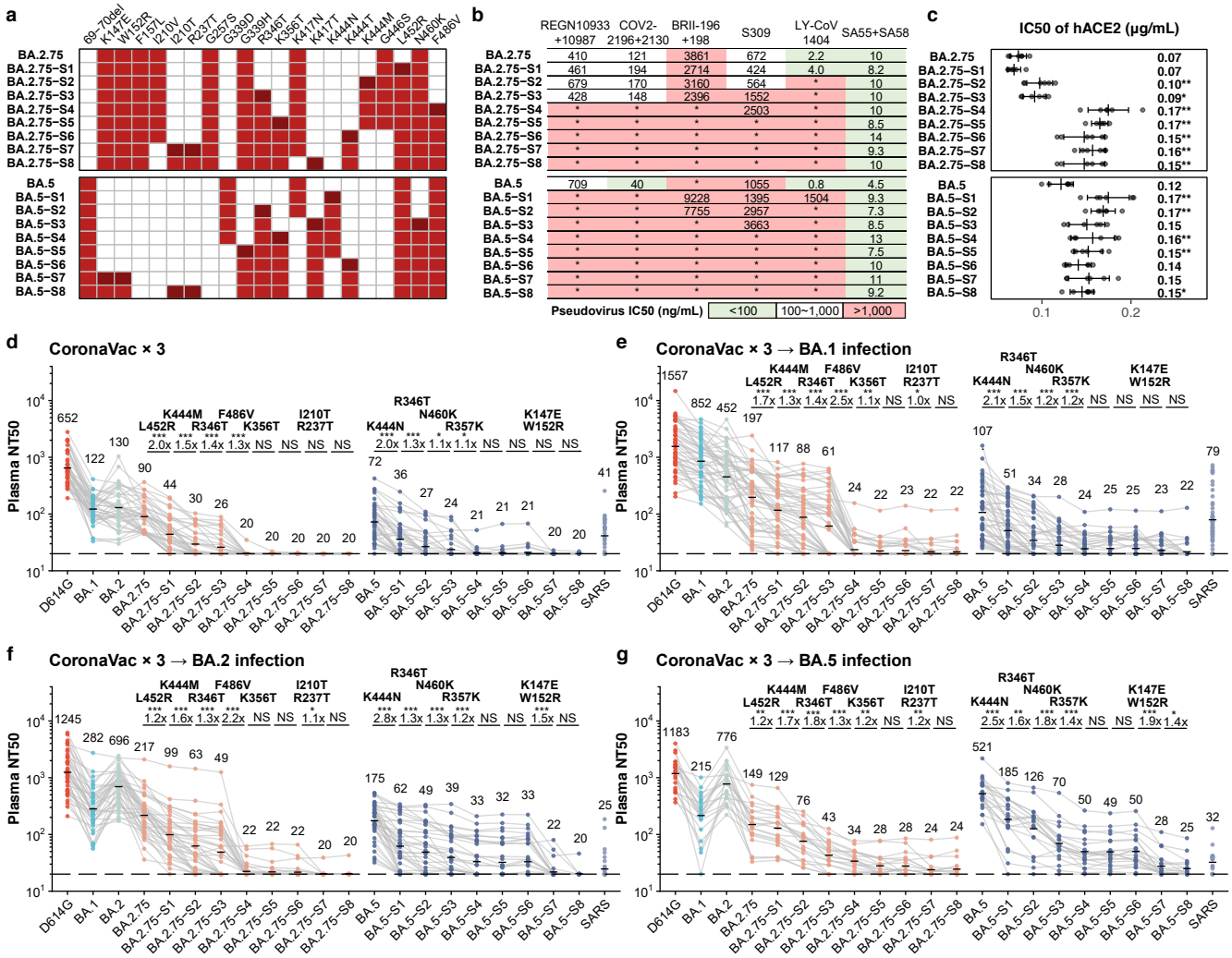

Fig. 5 | Accumulation of convergent escape mutations leads to complete loss of neutralization.
a, Mutations of multiple designed mutants that harbors key convergent escape mutations based on BA.2.75 and BA.5. b, IC50 of therapeutic mAbs and cocktails against pseudoviruses of designed mutants. green, IC50 ≤ 100ng/mL; white, 100ng/mL < IC50 < 1,000ng/mL; red, IC50 ≥ 1,000ng/mL; *, IC50 ≥ 10,000ng/mL. c, IC50 of hACE2 against the designed mutants. Error bars indicate mean±s.d. P-values were calculated using two-tailed Wilcoxon's rank-sum test. *, $p < 0.05$; **, $p < 0.01$; ***, $p < 0.001$. No label on variants with $p > 0.05$. d-g, Pseudovirus neutralizing titres against SARS-CoV-2 D614G, Omicron subvariants and designed mutants of plasma from vaccinated or convalescent individuals from breakthrough infection. d, Individuals who received 3 doses of CoronaVac (n = 40). e, Convalescents infected with BA.1 after receiving 3 doses of CoronaVac (n = 50). f, Convalescents infected with BA.2 after receiving 3 doses of CoronaVac (n = 39). g, Convalescents infected with BA.5 after receiving 3 doses of CoronaVac (n = 21). Key additional mutations harbored by each designed mutant are annotated above the points. The geometric mean titers are labeled. P-values are determined using two-tailed Wilcoxon signed-rank tests of paired samples. *, $p < 0.05$; **, $p < 0.01$; ***, $p < 0.001$; NS, not significant, $p > 0.05$. Statistical test are determined using two-tailed Wilcoxon signed-rank tests.

Extended Data Fig 1

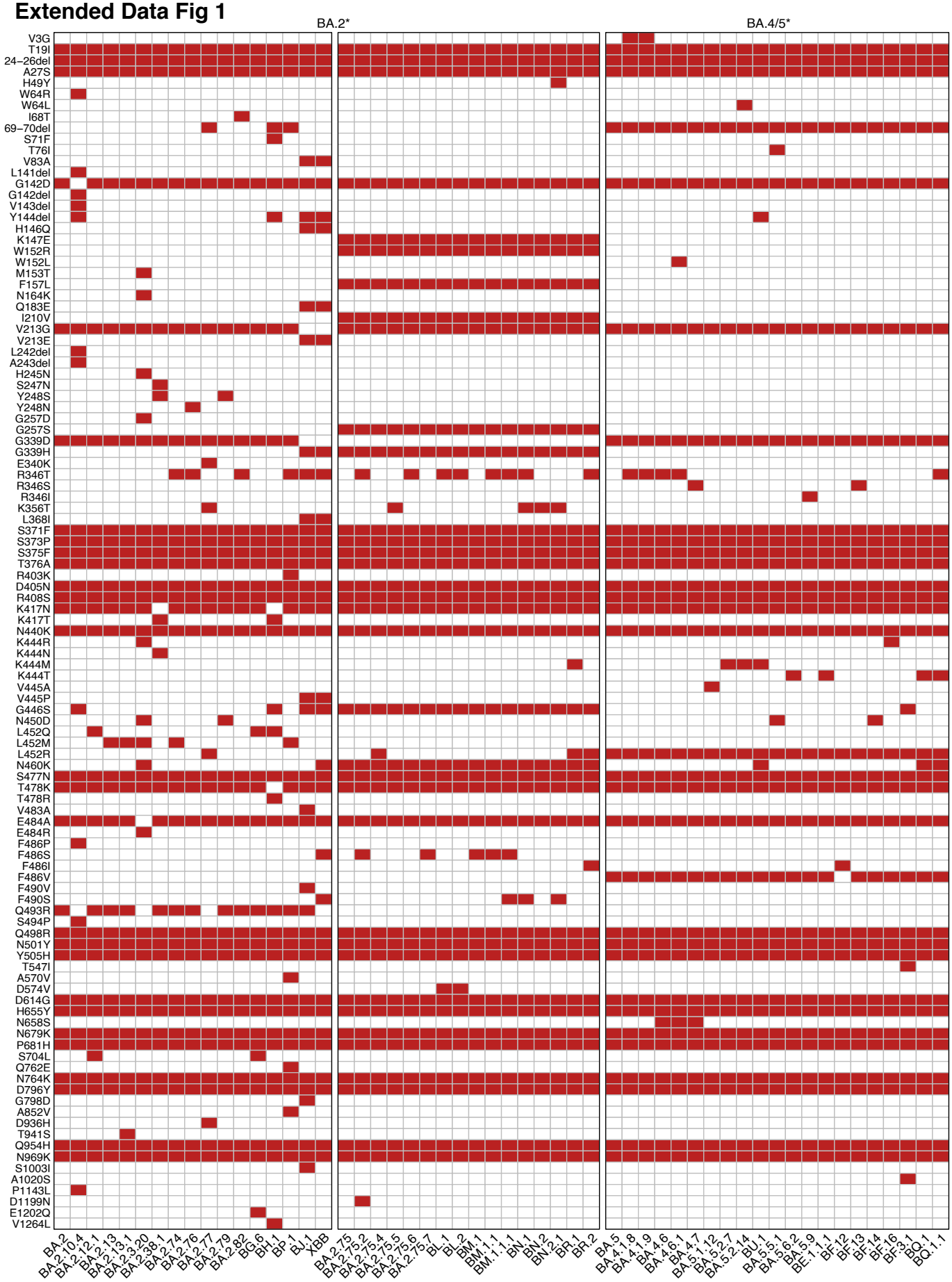

Extended Data Fig 2

a

Pango lineages	REGN 10933	REGN 10987	REGN10933 +10987	COV2-2196	COV2-2130	COV2-2196+2130	BRII-196	BRII-198	BRII-196+198	S309	DXP-604	LY-CoV 1404	SA58	SA55	SA55+ SA58	Additional RBD mutations
BA.2	*	590	821	4312	6.3	8.2	8530	8990	8610	852	219	0.9	5.1	7.2	7.8	
BA.2.38.1	*	*	*	3391	*	4736	4571	*	6212	876	33	1504	83	11	13	N417T+K444N
BA.2.74	*	2250	3211	3214	*	4300	6780	*	*	4943	191	2.6	293	4.2	6.9	R346T+L452M
BA.2.76	*	2336	4241	3162	*	5450	6021	*	*	6303	181	1.3	376	3.8	5.2	R346T
BA.2.77	*	657	584	4745	24	45	7209	*	*	*	259	0.9	*	4.6	6.6	K356R+L452R+E340K
BA.2.79	*	3051	7703	3587	3633	3019	3797	*	7767	1023	178	14	6.1	7.2	4.9	N450D
BA.2.80	*	2096	2201	4022	*	4133	5096	*	7202	*	206	1.0	*	6.2	10	R346T+K356R+E340K
BA.2.75	278	*	410	119	352	121	1730	6622	3861	672	5920	2.2	246	4.3	9.6	
BA.2.75.4	249	*	461	80	*	194	1448	*	2714	424	6553	4.0	254	4.0	8.2	L452R
BA.2.75.5	245	*	410	101	550	188	1590	*	3699	4780	6691	2.2	3305	4.8	9.1	K356T
BM.1	*	*	*	*	301	563	*	*	*	796	*	1.9	330	7.0	10.0	F486S
BA.4/5	*	520	709	*	23	40	7124	*	*	1055	6264	0.8	3.9	5.0	4.5	
BF.16	*	883	1863	*	48	79	4715	*	5507	1575	7505	2.7	6.7	3.3	6.0	K444R
BA.4.6	*	2195	4388	*	*	*	4356	*	8307	3543	4116	1.0	341	6.6	9.0	R346T
BA.4.7	*	1362	2420	*	*	*	3395	*	5209	2899	5189	1.4	598	3.8	6.8	R346S
BA.5.9	*	2701	3498	*	*	*	4023	*	7695	4780	8360	1.3	404	4.8	8.7	R346I
BA.5.5.1	*	1936	2963	*	*	*	5023	*	8236	1293	6807	5.1	17	6.0	8.0	N450D
BA.5.2.7	*	*	*	*	*	*	3701	*	6502	1419	6263	25	63	4.3	9.6	K444M
BA.5.1.12	*	*	*	*	1843	4818	3505	*	4849	1752	8268	98	3.6	3.4	4.6	V445A

Pseudovirus IC50 (ng/mL): <100 | 100~1,000 | >1,000

b

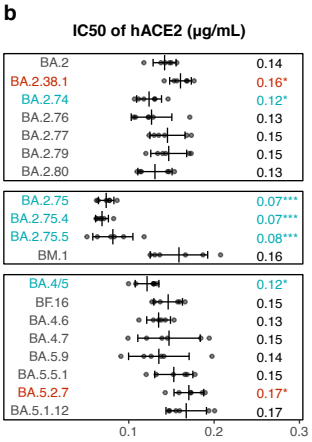

c

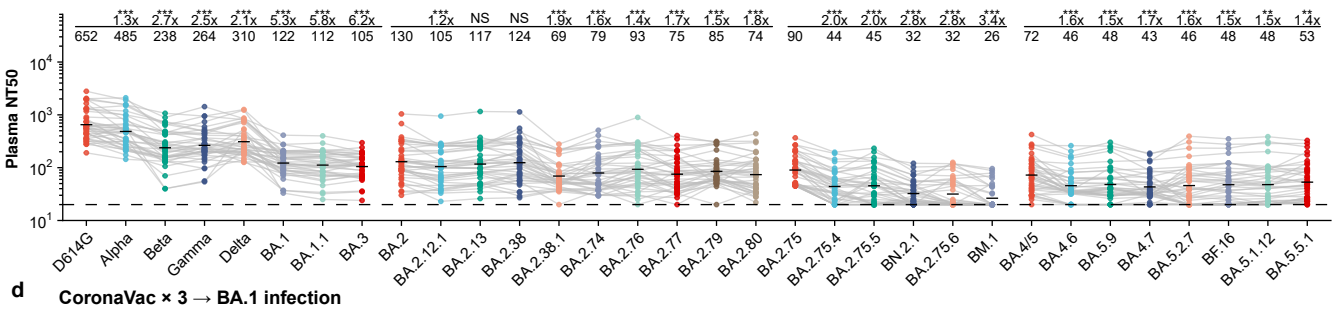

d

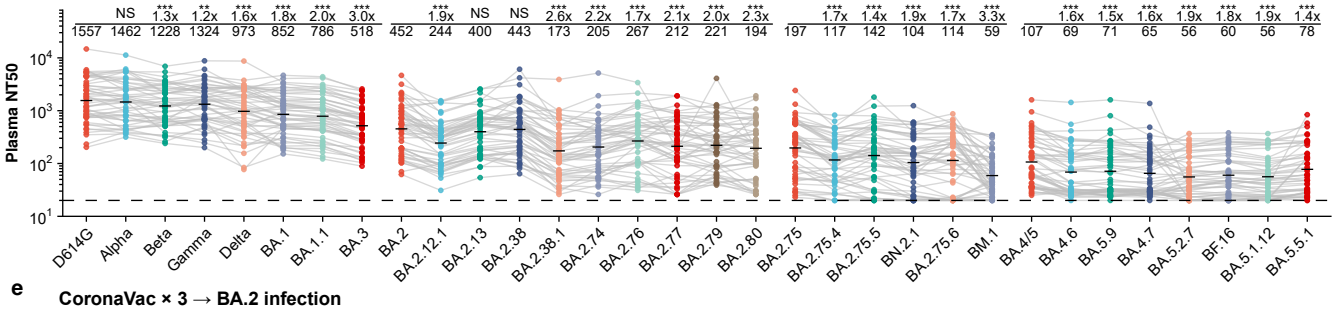

e

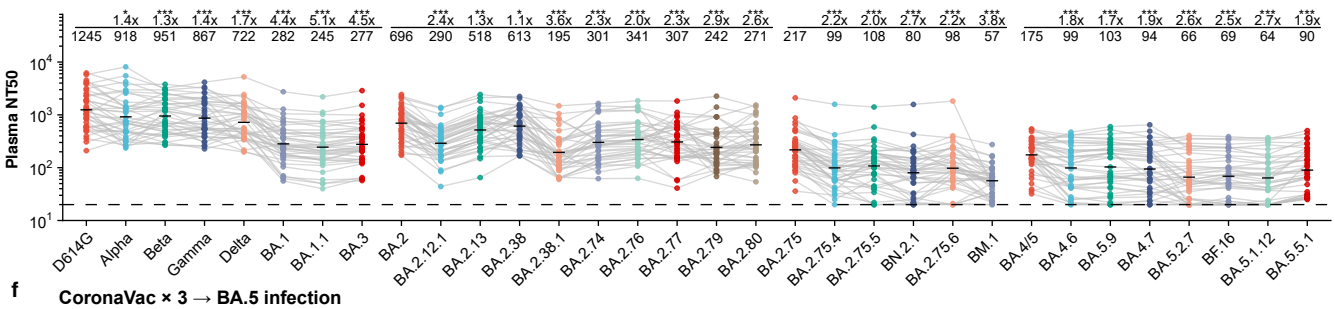

f

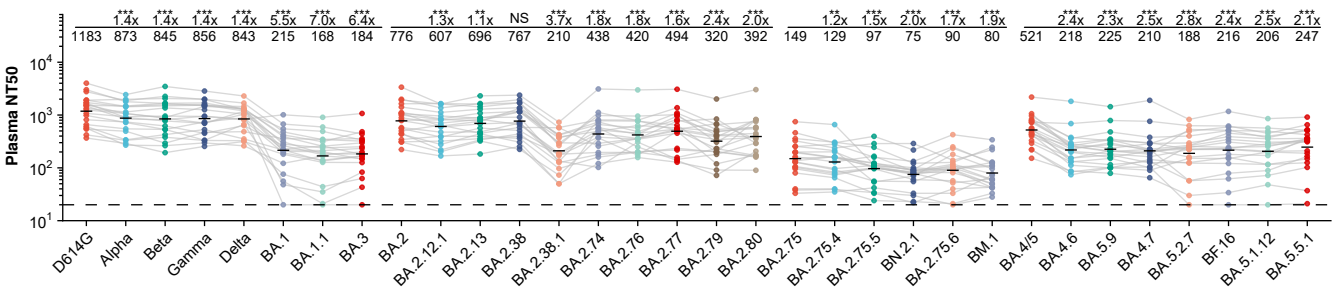

Extended Data Fig 3

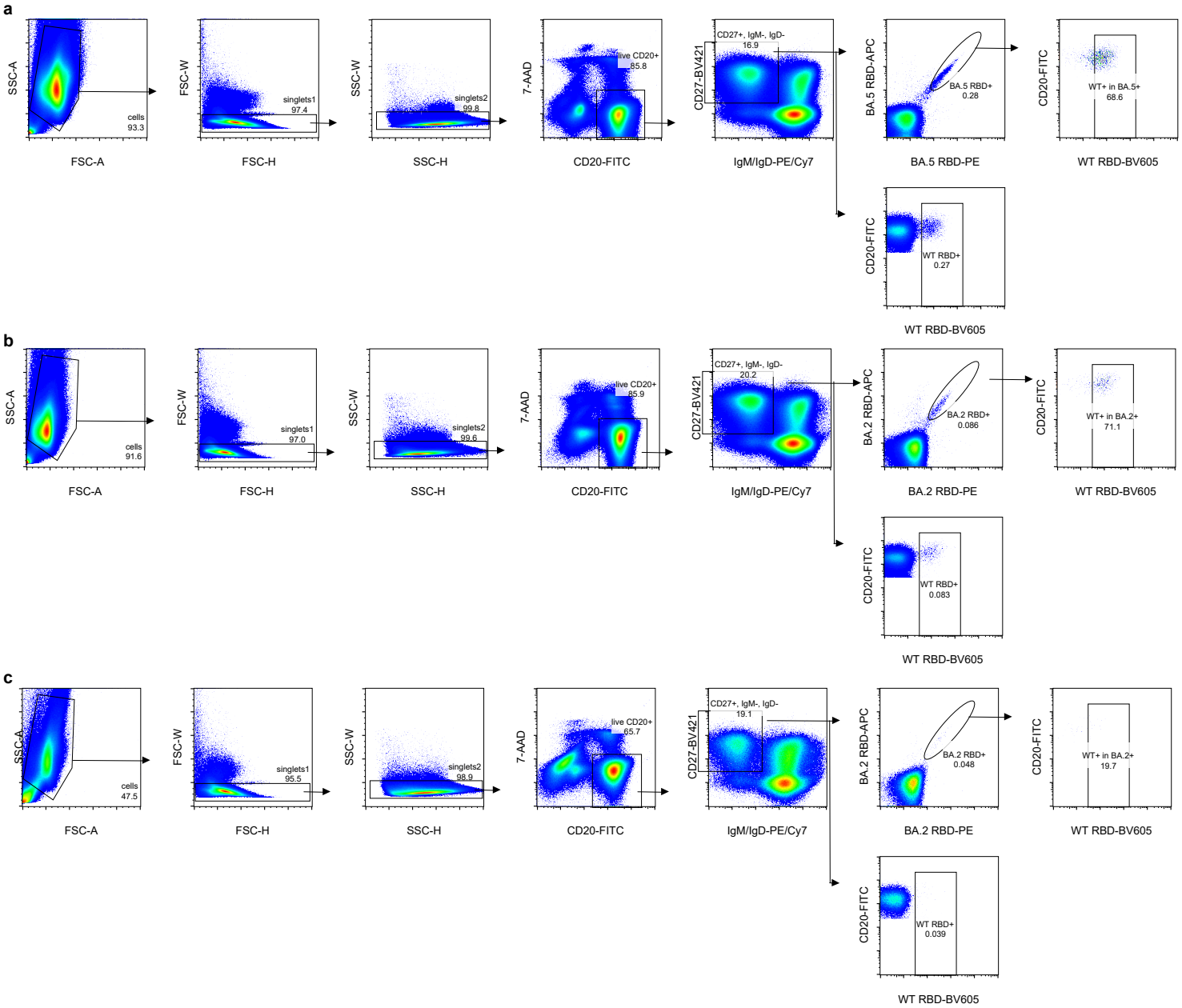

Extended Data Fig 4

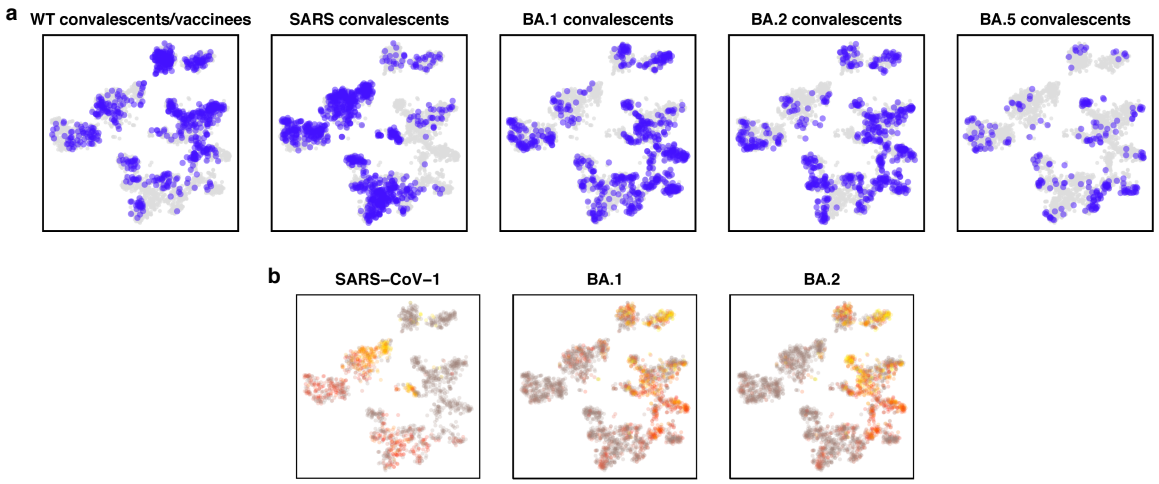

Extended Data Fig 5

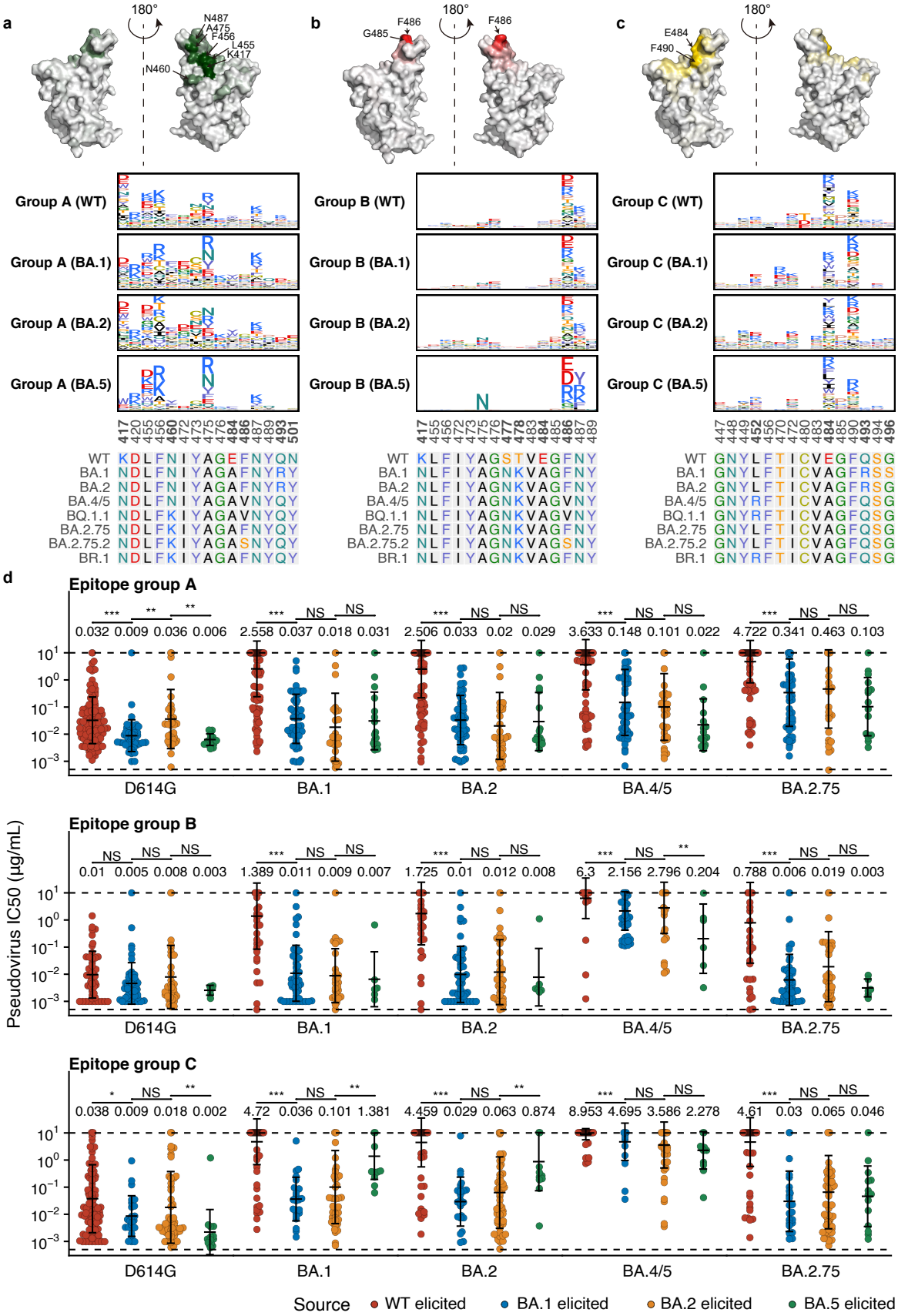

Extended Data Fig 6

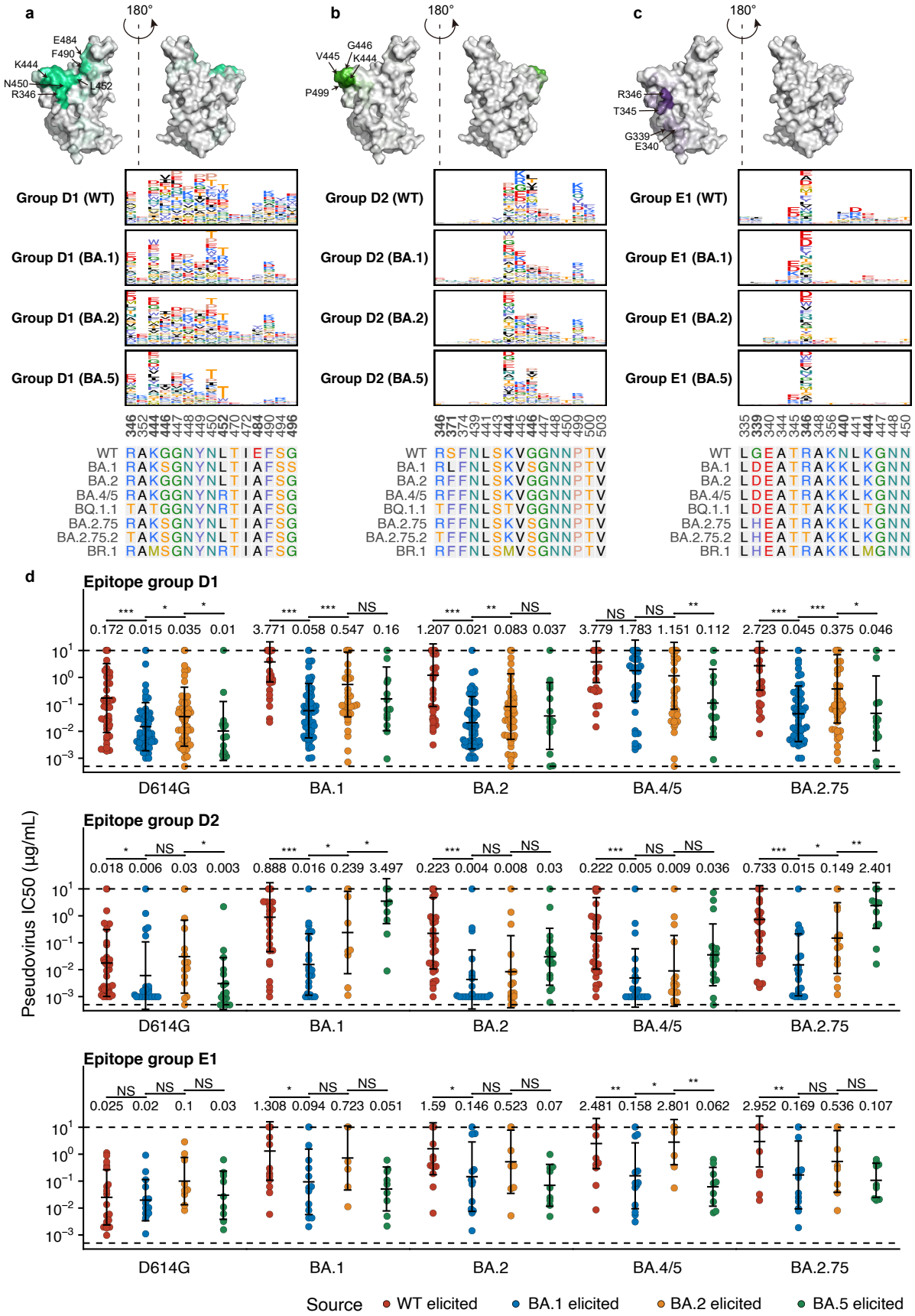

Extended Data Fig 7

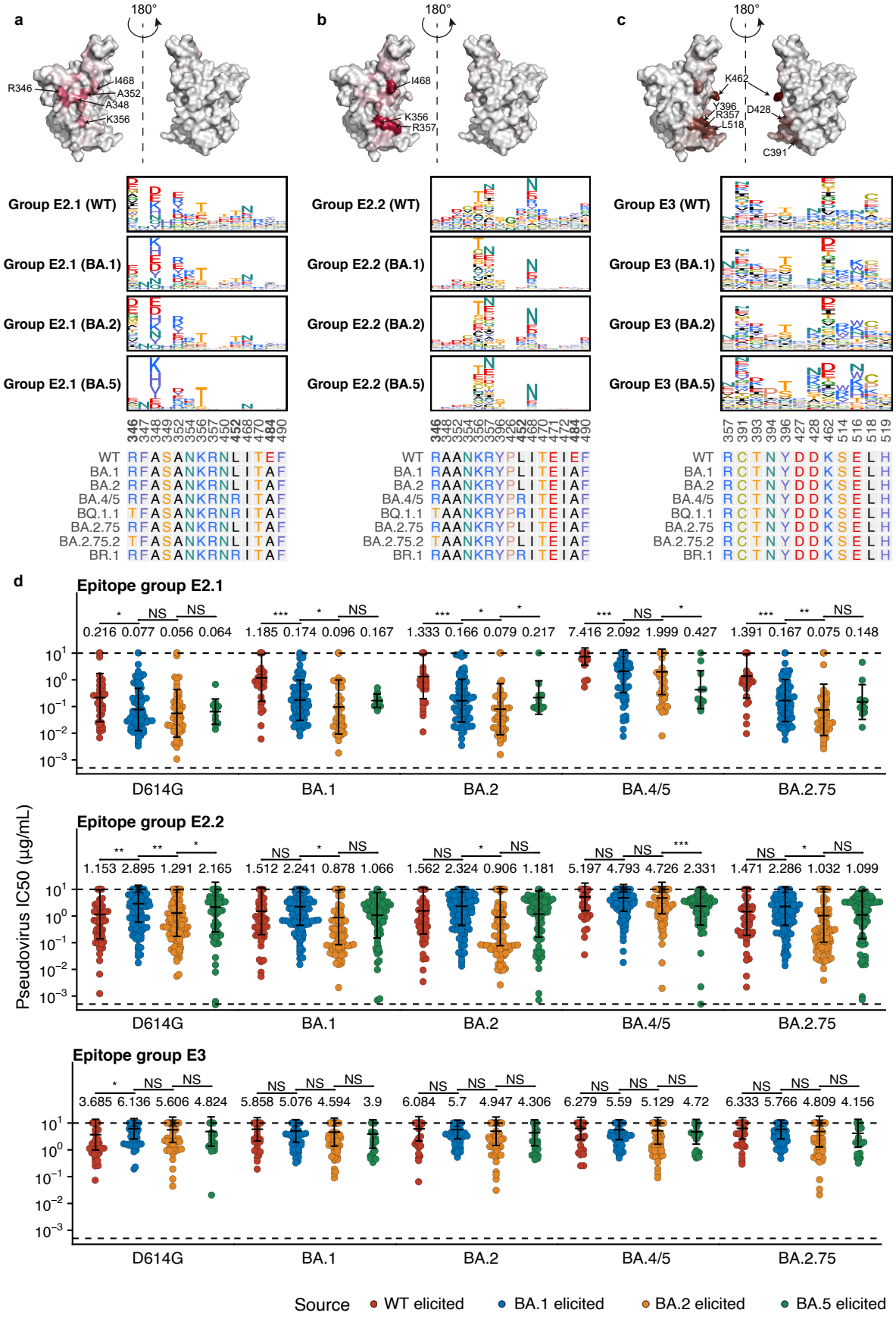

Extended Data Fig 8

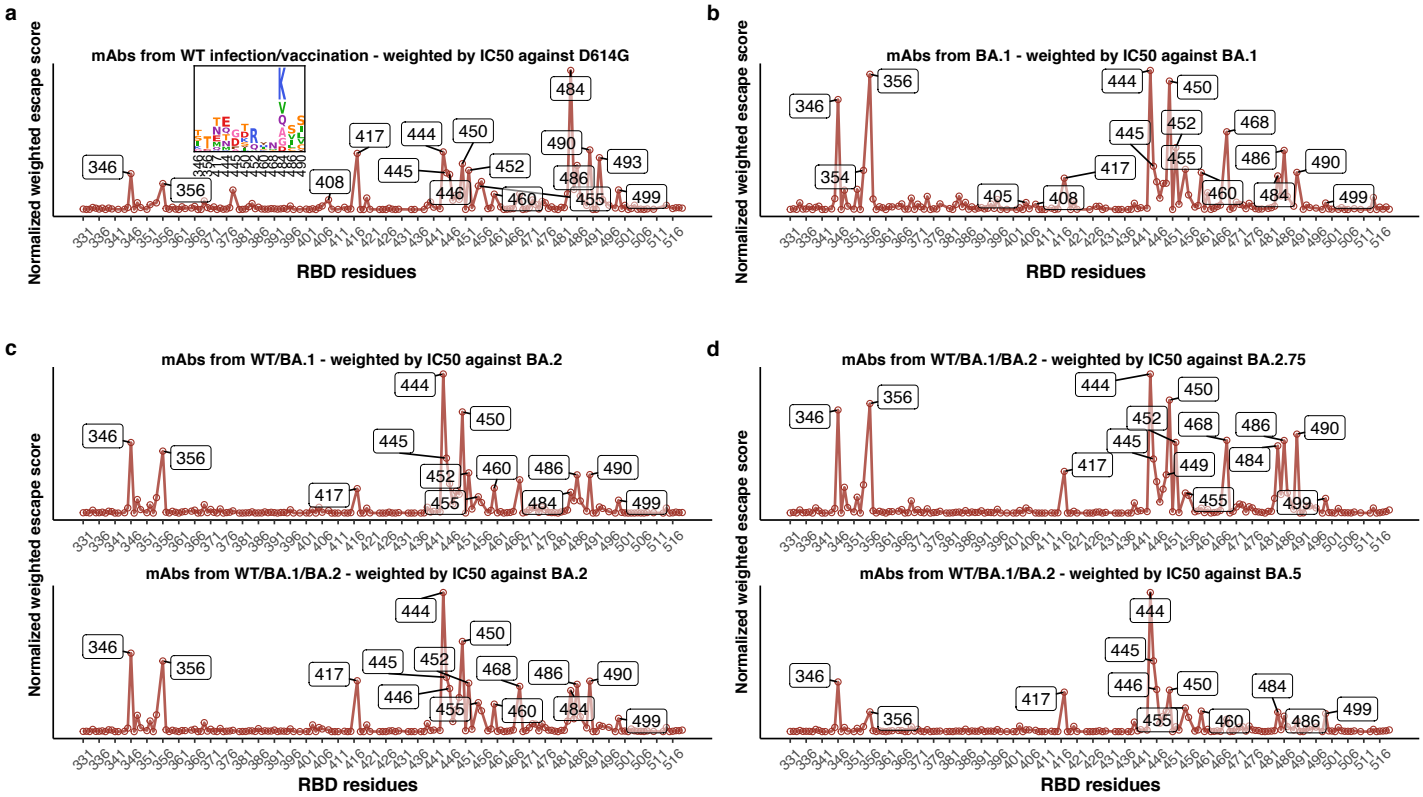

Extended Data Fig 9

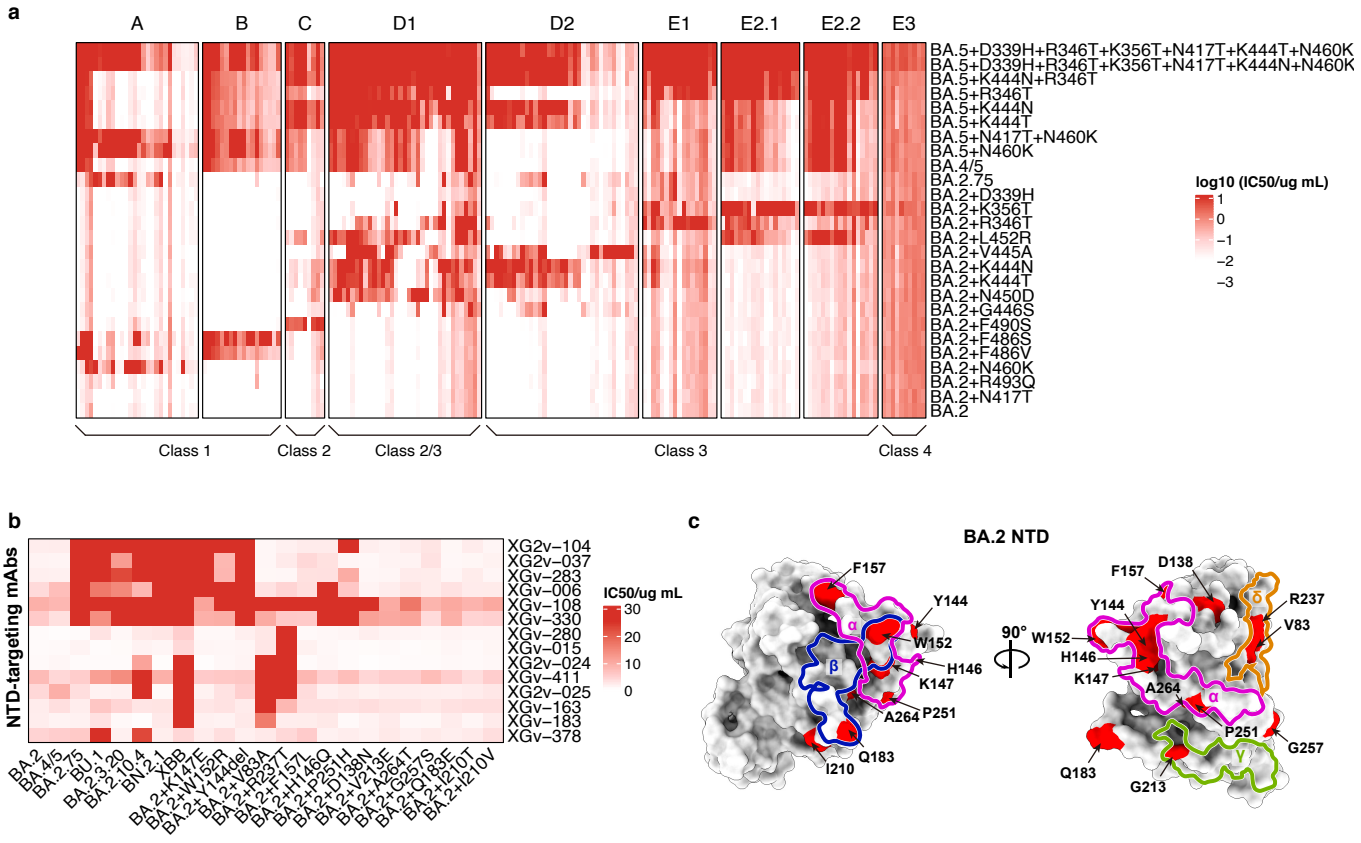
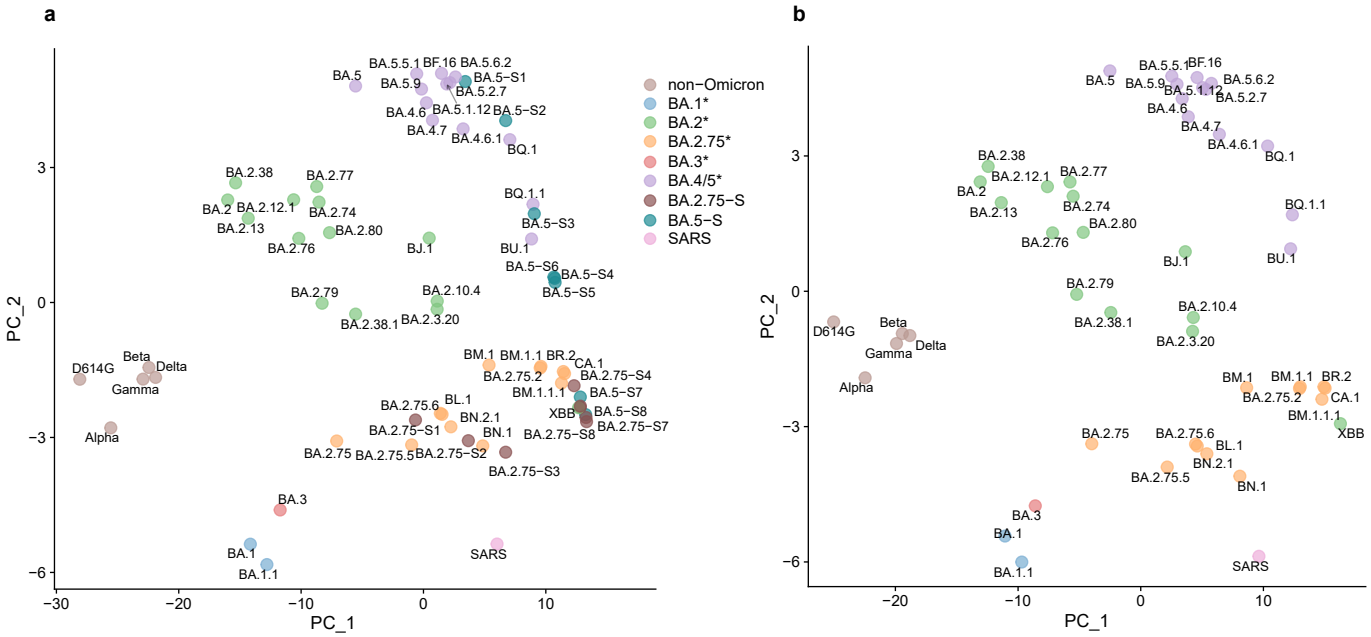
Extended Data Fig 10